Dynamical Analysis of Terahertz Quantum Cascade Lasers

Önder, Denizhan Ekin

2023

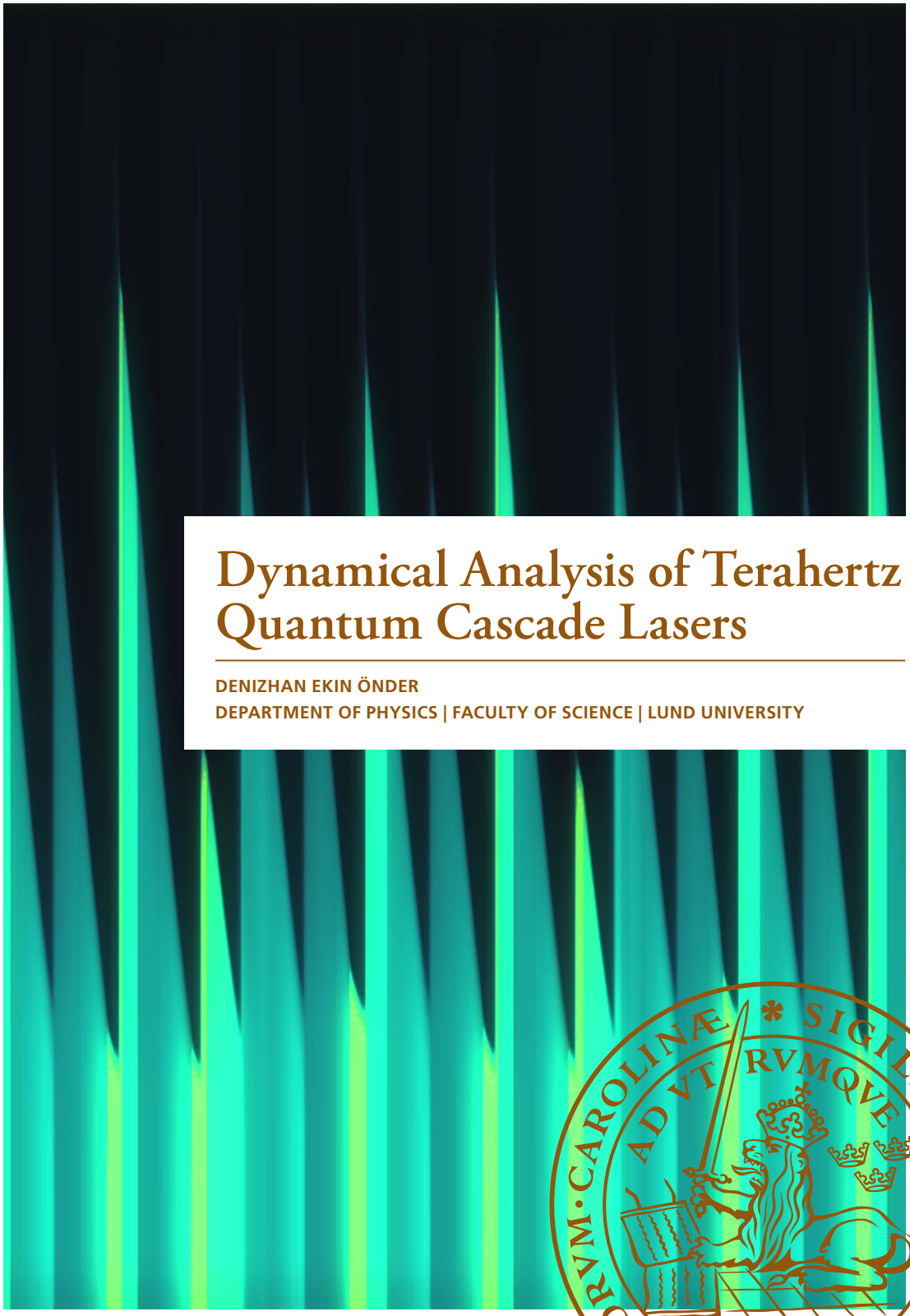

Dynamical Analysis of Terahertz Quantum Cascade Lasers

DENIZHAN EKIN ÖNDER
DEPARTMENT OF PHYSICS | FACULTY OF SCIENCE | LUND UNIVERSITY

Printed by Media-Tryck, Lund 2023 NORDIC SWAN ECOLABEL 3041 0903

Faculty of Science
Department of Physics

ISBN 978-91-8039-567-0

Dynamical Analysis of Terahertz Quantum Cascade Lasers

Dynamical Analysis of Terahertz Quantum Cascade Lasers

by Denizhan Ekin Önder

LUND
UNIVERSITY

Thesis for the degree of Doctor of Philosophy
Thesis advisor: Prof. Andreas Wacker
Faculty opponent: Prof. Carlo Sirtori

To be presented, with the permission of the Faculty of Scienceof Lund University, for public criticism in the Rydberg lecture hall at the Department of Physics on Wednesday 24th of May 2023 at 13:00.

Organization
LUND UNIVERSITY

Department of Physics
Box 118
221 00 Lund
Sweden

Author(s)
Denizhan Ekin Önder

Document name
DOCTORAL DISSERTATION

Date of disputation
2023-05-24

Sponsoring organization

Title and subtitle
Dynamical Analysis of Terahertz Quantum Cascade Lasers

Abstract
This thesis focuses on various aspects in terahertz quantum cascade lasers such as high temperature performances, electrical instabilities and chaos. In the first part of the thesis, an introduction to the topic and the non equilibrium Green's function package applied is given with particular emphasise on the inhomogeneous domain model and the chaos theory. In addition, new results regarding the high temperature operation of low frequency terahertz quantum cascade lasers are presented. In the second part, the related research articles are shown.

Paper I shows numerical simulations demonstrating the first autonomous terahertz quantum cascade laser exhibiting chaos.

Paper II provides a detailed analysis of the current record-holding terahertz quantum cascade lasers operating around 4 terahertz. A new design is suggested which should operates at an even higher temperature of 265 K.

Paper III analyses the spectral behaviour of the output light generated by oscillating field domains in direct cooperation with the experiment. The overall behaviour is related to the phenomenological boundary conductivity and the external capacitance.

Key words
Terahertz, quantum cascade lasers, electric field domains, chaos, simulation

Classification system and/or index terms (if any)

Supplementary bibliographical information

Language
English

ISSN and key title

ISBN
978-91-8039-567-0 (print)
978-91-8039-566-3 (pdf)

Recipient's notes

Number of pages
135

Price

Security classification

Signature _____ Date 2023-04-03

Dynamical Analysis of Terahertz Quantum Cascade Lasers

by Denizhan Ekin Önder

LUND
UNIVERSITY

Cover: Field domain image is adapted from Fig. 3.3. Credit: Denizhan Ekin Önder

Faculty of Science, Department of Physics
ISBN: 978-91-8039-567-0 (print)
ISBN: 978-91-8039-566-3 (pdf)

Printed in Sweden by Media-Tryck, Lund University, Lund 2023

Dedicated to my mother, father and my dear Irja

Contents

List of publications iii

Acknowledgements **v**

Popular summary **vii**

Populärvetenskaplig sammanfattning **ix**

I Research context

1 Introduction **3**
1.1 Operation Principles of Lasers 4
1.2 THz Quantum Cascade Lasers 5
1.3 Negative Differential Conductivity 9
1.4 Motivation of this thesis 11

2 The Model **13**
2.1 General Hamiltonian 13
2.2 Computational scheme of the NEGF package 16

3 Dynamics of Electric Field Domains **21**
3.1 Travelling Electric Field Domains 22

4 Chaos **31**
4.1 Modelling Chaos 32
4.2 Examples of Complex Systems 44

5 Low Frequency THz Quantum Cascade Lasers 47
5.1 Applications of the NEGF Package 48
5.2 High performing THz QCLs at low frequencies 57

6 Summary and Outlook 59

A 61
A.1 Rate equations and gain medium 61
A.2 Extracting results from the NEGF package 64

II Research Papers

Scientific publications
Author contributions . . . . . .
Paper I: Chaotic Behaviour of Quantum Cascade Lasers at Ignition . .
Paper II: Analysis of High-Performing Terahertz Quantum Cascade Lasers
Paper III: Frequency Modulations due to Domain Dynamics in Terahertz Quantum Cascade Lasers . . . . . .

List of publications

This thesis is based on the following publications, referred to by their Roman numerals:

I **Chaotic Behaviour of Quantum Cascade Lasers at Ignition**

D. E. Önder, A. A. S. Kalaee, D. O. Winge, A. Wacker
Communications in Nonlinear Science and Numerical Simulation, **103**, 105952 (2021)

II **Analysis of High-Performing Terahertz Quantum Cascade Lasers**

Viktor Rindert, Ekin Önder, Andreas Wacker
Physical Review Applied **18**, L041001 (2022), [Letter Section]

III **Frequency Modulations due to Domain Dynamics in Terahertz Quantum Cascade Lasers**
E. Önder, D. O. Winge, M. Franckié, A. Forrer, U. Senica, G. Scalari, and Andreas Wacker
Journal of Applied Physics, **133**, 123101 (2023), [Featured article]

Acknowledgements

I hereby owe my deepest gratitude and thanks to my supervisor Andreas Wacker. I had a unique experience with my PhD, not only learned about being a scientist but also what kind of a person I wanted to be. Thank you for accepting me as your student and introducing me with wonderful physicists around the world. Also, I would like to thank you for your support and understanding in hard times such as during the Covid-19. I appreciate everything I learned from you and I hope I will have the chance to work with you in a foreseeing future again.

I also like to thank to David Winge and Martin Franckié for their enormous support of helping me both as a colleague and as a friend. Your passion and success in science inspired me and gave me strength in times when I struggled the most. I also like to thank Alex Arash Sand Kalaee for his friendship. I really enjoyed to work together with all of you. A special thanks to Viktor Rindert. I really enjoyed to work with you and thank you for your friendship.

I like to thank my co-supervisors Peter Samuelsson and Claudio Verdozzi for your support and kindness. I like to thank Lila, Timo, Gunnar, Tor, Björn, Asimina, Rezvan and Drilon. Even though it is quite hard to start a life in a new country I did not know, from the my first day to now I made me feel at home. A special thanks to Mattias, we started at the same time and we are finishing in the same week. We laughed, cried and experienced together. I wish you the best of luck and happiness in your wedding and your future.

I also like to thank Jakob and Andrea. I learned a lot from you and I am very happy to meet with you.

I would of course like to thank you Marcus. I really enjoyed the times when we played together and ate kebab together. I really hope to do a another blues jam

with you in the future.

I would also like to thank everybody in the mathematical physics division. You made me feel like at home during my time and I am most gratitude. Do not be afraid, Summer is on the horizon.

Popular summary

Over the last century, artificial light became eminent for mankind with widespread usage ranging from technological applications to entertainment. Such as Star Wars movies have changed the perspective of an entire generation on science. Now, a general view of having a PhD in physics represents a person closer to invent the light saber. To be honest, that is our dream too. Unfortunately, in this study we studied only the boring part of the light, it's technological versions.

The physics of light has attracted attention for quite some time. A particular example is Newton's interest on light corpuscles. He thought that the light propagation is caused by light particles and named them as corpuscles. He suggested that these light particles have a certain speed and in contact with any rigid surface, these particles shall obey Newtonian mechanics. Even though his theories were quite close to the modern approach, he did not take into account that light propagates also as waves. The introduction of the electromagnetic (EM) wave is first formulated by a Scottish physicist and mathematician James Clark Maxwell. He added the displacement current to Ampere's law and the solution of his equations were waves which travel close to the speed of light. This was a historical moment for scientific development since the Maxwell's equations are the beginning of an era with enormous technological developments. One example is that the invention of the telegraph helped Titanic to send an SOS signal after it's collision with the iceberg and Rose survived. Soon after the introduction of the EM waves, the first EM spectrum is introduced by a German physicist Heinrich Hertz and led us to catalog light by its frequency. Now we know, from MRI machines to visible colors and light from far distant galaxies, different frequencies of light represent different natural perspectives in the universe.

With the invention of quantum mechanics our fundamental knowledge on the

micro universe is expanded. Now, with all these technological advancements we could produce light in a very wide range in the EM spectrum. In this work, we study on a device called quantum cascade laser. These unique devices are used to produce light in the far to mid infrared range between 1.2 to 100 terahertz depending on their design. This provides them to be useful in technological applications in the related frequency ranges such as gas detection, military defence systems or even medical fields of breath analysis.

One of the biggest challenges now is the achievement of high temperature operation of quantum cascade lasers over a wide range of frequencies in the terahertz. Here, we suggested new designs where the thermoelectrical cooling is possible within the entire range between 2 to 4 terahertz. This enables more designs to be applicable in technological usage. Another interesting outcome is that we show chaos in the output signal of a quantum cascade laser. Eventually, I did not manage to build a light saber, but I provide more knowledge on chaos theory. I hope this would help to understand which path the water drop will follow in Jeff Goldblum's hand in Jurassic Park I.

Populärvetenskaplig sammanfattning

Under det senaste århundradet har artificiellt ljus kommit att bli oerhört betydelsefullt för mänskligheten. Användningsområdet för artificiellt ljus är brett och innefattar allt från tekniska tillämpningar till underhållning. Bara det att Star Wars-filmer har förändrat en hel generations perspektiv på vetenskap, säger en hel del. En allmän syn på en person som har en doktorsexamen i fysik är att vi jobbar med att uppfinna ljussabeln. För att vara helt ärlig så är det en dröm många av oss har. Tyvärr så kommer denna studie bara utforska den tråkiga delen av ljuset, den tekniska delen.

Ljusets beteende har uppmärksammats relativt länge. Ett särskilt exempel är Newtons intresse för ljuskroppar. Han antog att ljusets utbredning orsakas av ljuspartiklar och benämnde dem som blodkroppar. Han föreslog att dessa lätta partiklar har en viss hastighet och i kontakt med vilken stel yta som helst, ska dessa partiklar lyda Newtons mekanik. Även om hans teorier låg ganska nära det moderna förhållningssättet, tog han inte hänsyn till att ljus även sprider sig likt vågor. Införandet av den elektromagnetiska (EM) vågen formulerades först av en skotsk fysiker och matematiker James Clark Maxwell. Han lade till förskjutningsströmmen till Amperes lag och resultatet av hans ekvationer var vågor som färdas nära ljusets hastighet. Detta var ett historiskt ögonblick för vetenskaplig utveckling eftersom Maxwells ekvationer var början på en era med enorm teknisk utveckling. Ett exempel på det är att uppfinningen av telegrafen hjälpte Titanic att skicka en SOS-signal efter kollision med isberget och Rose överlevde.

Strax efter introduktionen av EM-vågorna introduceras det första EM-spektrumet av en tysk fysiker, Heinrich Hertz, som hjälpte till att katalogisera ljus efter dess

frekvens. Nu vet vi att, från MRI-maskiner, synliga färger och till ljus från långt avlägsna galaxer, olika frekvenser av ljus representerar olika naturliga perspektiv i universum.

Med kvantmekanikens upptäckt utökas vår grundläggande kunskap om mikrouniversum. I och med alla dessa tekniska framsteg kan vi producera ljus i ett mycket brett spektrum i EM-spektrumet. I detta arbete studerar vi en enhet som kallas kvantkaskadlaser. Dessa unika enheter används för att producera ljus i det långt till mitten infraröda området mellan 1,2 till 100 terahertz beroende på deras design. Detta gör att de kan vara användbara i tekniska applikationer inom de relaterade frekvensområdena, såsom gasdetektering, militära försvarssystem eller till och med medicinska områden av andningsanalys.

En av de största utmaningarna nu är uppnåendet av högtemperaturdrift av kvantkaskadlasrar över ett brett spektrum av frekvenser i terahertz. Här föreslår vi nya konstruktioner där den termoelektriska kylningen är möjlig inom hela området mellan 2 till 4 terahertz. Detta gör att fler mönster kan användas inom tekniska användningsområden. Ett annat intressant resultat är att vi visar kaos i utsignalen från en kvantkaskadlaser.

I slutändan lyckades jag inte bygga en ljussabel, utan men jag ger er mer insyn och kunskap om kaosteori. Jag hoppas att detta kommer hjälpa till att förstå vilken väg vattendroppen kommer att följa i Jeff Goldblums hand i Jurassic Park I.

Part I

Research context

Chapter 1

Introduction

The quantum cascade laser (QCL) was first realized in the Bell Laboratories by Jerome Faist et. al. in 1994 [1] with the lasing wavelength of 4.2 μm. The study promised further technological applications in the far to mid infrared (IR) region in the electromagnetic (EM) spectrum. Following the introduction of the QCLs, both experimental and theoretical interests are elevated significantly. This is followed by the achievement of continuous wave operation at room temperature by Beck et. al. in 2002 [2] around mid IR. Reaching room temperature was a big step towards the technological applicability where mid IR sources are widely used. These areas are gas detections, quality controls and even military technologies such as defence and security systems [3, 4, 5, 6]. Around the same year, the first terahertz (THz) QCL operation in pulsed mode was achieved by Köhler et. al. [7]. Following this study, THz QCLs became viable sources between 1.5 and 6 THz. However, the struggle was the achievement of continuous wave operation at room temperature while the highest operation temperature of 250K in pulse mode is experimentally observed by Ref. [8]. Based on this model, we also suggested a new study in Paper II showing that the achievement of operation at even a higher temperature of 265 K is possible. Now, QCLs are viable sources of generating radiation between 1.2 to 100 THz [9] and their technological applications are possible either in room temperature in IR or via thermoelectrical cooling in THz.

In classical laser diodes, the generation of a single photon is based on interband transitions [11]. A high energy electron in the conduction band combines with a hole in the valance band and the energy of the emitted light resulting from this

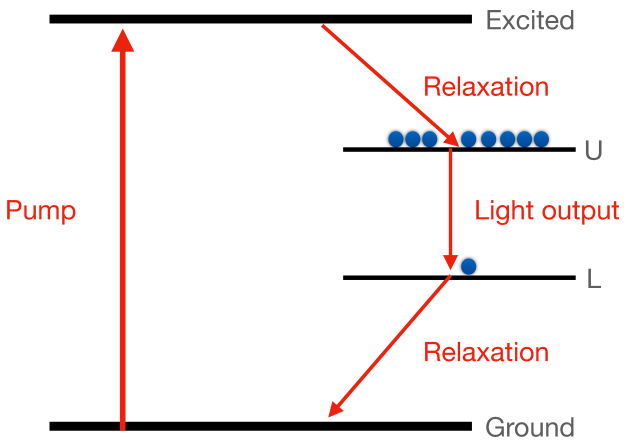

Figure 1.1: Four level laser diagram including ground, excited, upper (U) and lower (L) states. Arrows represent the direction of pumping, emission of light and relaxations. The figure is adapted from Ref. [10].

combination is calculated by the energy difference of the band gap by the material of use. This restricts the flexibility to vary energies of the emission and thus limits the frequency of the output light. In quantum cascade lasers, the design of an optical medium is based on quantum wells/barriers to trap the particles [12, 13]. The outcome of the trapping electrons results in discrete energy states due to the quantum confinement. These discrete energy levels are used as optical levels to produce optical power[14, 15, 16]. Varying the sequence and width of the wells/barriers change the energy of these discrete levels. This provides more flexibility to achieve lasing field in different frequencies via the same composition of semiconductor materials. In this thesis, I show my contributions to the ongoing researches in THz QCLs with studying temperature performance analysis as well as the electric field domains and the theory of chaos.

1.1 Operation Principles of Lasers

For a system with electrons excited from a lower energy state to a higher one, stimulated emission of light occurs due to the energy transfer of the excited electrons to a light field. This is usually referred as the laser medium. For a simplified working principle of a laser medium, Fig. 1.1 shows an illustration of a four level scheme [10]. This is one general example to show the mechanisms of pumping, lasing and

injection/extraction of the electrons between the energy levels.

Here in Fig. 1.1, first the atoms are pumped to an excited state with higher energy. This pumping mechanism can be the light emission from an external source, an applied electric potential or any other sources (e. g. excitation from electrical discharge). Providing such an external source excite the electrons in the ground state and transfer them to the excited level (i. e. via stimulated absorption)[10, 17]. This process refers to the pumping of the electrons and the direction of the transfer is shown by the vertical arrow pointing upwards.

After the particles reach to the excited level, they quickly relax to the upper laser level "U" with losing their energy and start accumulating i. e. creating inverted population. These electrons may stay longer in the upper level depending on their scattering probability. This is followed by the transition of the electrons to the lower level "L" by either scattering or emission of the light. This transition occurs relatively slower than the relaxation time. In case of photon emission, these photons will create an optical gain. Finally, particles quickly depopulate "L" and relaxes to the ground state.

To trap the photons, since they move with the speed of light, inserting mirrors on the sides of the system will create cavity modes [10]. This results in building power regarding the multiplication of the trapped photons, creating a gain medium. If we consider the leakage from the mirrors as losses, the emission of light occurs when the optical gain is higher than the losses.

To summarize, the main idea to operate an efficient laser is depending on keeping the particles long enough in the upper laser level to achieve higher population and quickly depopulate the lower laser level. The trapped photons between the mirrors will be amplified yielding a build up of optical power i. e. a functioning laser device.

1.2 THz Quantum Cascade Lasers

The operation of the QCLs are based on intersubband transitions in the conduction band [16]. The carrier transport in QCLs is based on one type of charge; electrons. Therefore, they are also known as unipolar lasers [19]. In QCLs, using bulk semiconductors in the active region design is not an option, instead, a heterostructure is formed by using periodic repetitions of thin layers with using different semiconductor material compositions [14]. These periodic repetitions

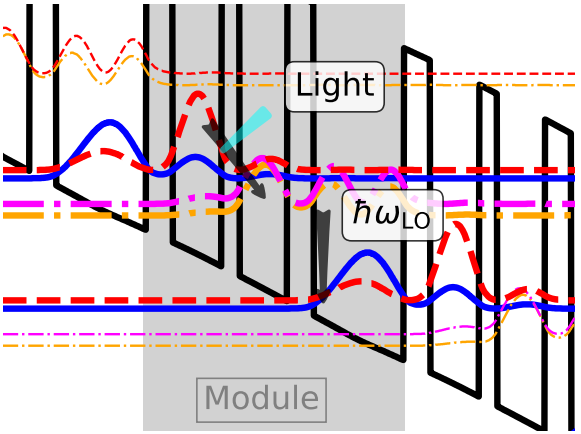

Figure 1.2: Cascading conduction band diagram of a terahertz QCL taken from Ref. [18]. Each module consists of three wells and three barriers represented by black solid lines. The probability density of the wavefunctions are plotted and showing the upper, the lower and the extraction/injection levels with solid, dashed and dashed dot curves respectively. Diagonal arrow represents the lasing transitions and the vertical arrow represent the longitudinal optical phonon transition.

form a cascading design based on barriers and wells in the conduction band as shown in Fig. 1.2. Here, the thickness of the layers settles the location of the energy levels. Varying the emission frequency can be done easily by only changing the layer thicknesses and sequences. Thus, they provide generation of light in a broader range of far to mid infrared region in the electromagnetic (EM) spectrum. In this thesis, we focus on the Terahertz (THz) range and the THz QCLs have emission frequencies between 1.2 and 5.4 THz [20, 21, 22]. This is due to the small energy separation between the upper and lower levels.

With applying an external bias, which provides the tilted alignment, particles first are injected to the injection level (blue solid curves) as seen in Fig. 1.2. The alignment of the injection and the upper laser level (red dashed curves) allows carriers to resonant tunnel to the upper laser level. Here, in the absence of any scattering mechanism, carriers persist long enough to achieve inverted population. Following with the stimulated emission of the carriers to the lower laser level (magenta dashed dot curves), lasing transition occurs. This is followed by the quick depopulation of the lower laser states by the extraction level (orange dashed dot curves) to

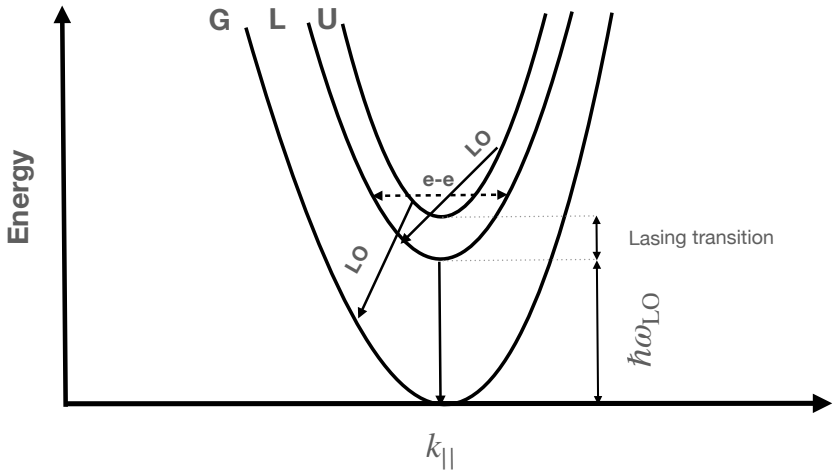

Figure 1.3: Illustration of the three subbands of upper (U), lower (L) and ground (G) in the conduction band. The longitudinal optical phonon transitions as well as the lasing transition ranges are shown by arrows. Dashed arrows represents the electron electron scatterings.

assure the inversion. The extraction of these carriers by longitudinal optical (LO) phonon transition to the injection level in the neighbouring module is followed by the pumping of the carriers again and the same processes are repeated.

1.2.1 Different Structure Designs

Extraction Schemes

The quick depopulation of the lower laser level is the key point to sustain enough inversion. In conventional THz QCLs, the energy separation between the lower laser and the ground levels are typically around $35 - 37$ meV. This is approximately the same energy of the LO phonons with $\hbar\omega_{LO} = 36$. The depopulation mechanism is usually established by the scattering of the longitudinal optical (LO) phonons as seen in Fig. 1.3. This is either done by placing the lower laser and the injection level in the same well, i. e. direct LO phonon extraction (see Fig. 1.4(a)), or adding an additional extraction barrier. Thus, extraction is done by the resonant tunneling of the carriers to an additional energy level in the neighbouring well (see Fig. 1.4(b)). This additional energy level is usually referred to the extraction level. When the extraction level resonates with the lower laser level, carriers tunnel and depopulate the lower laser level. This is followed by their de-excitations

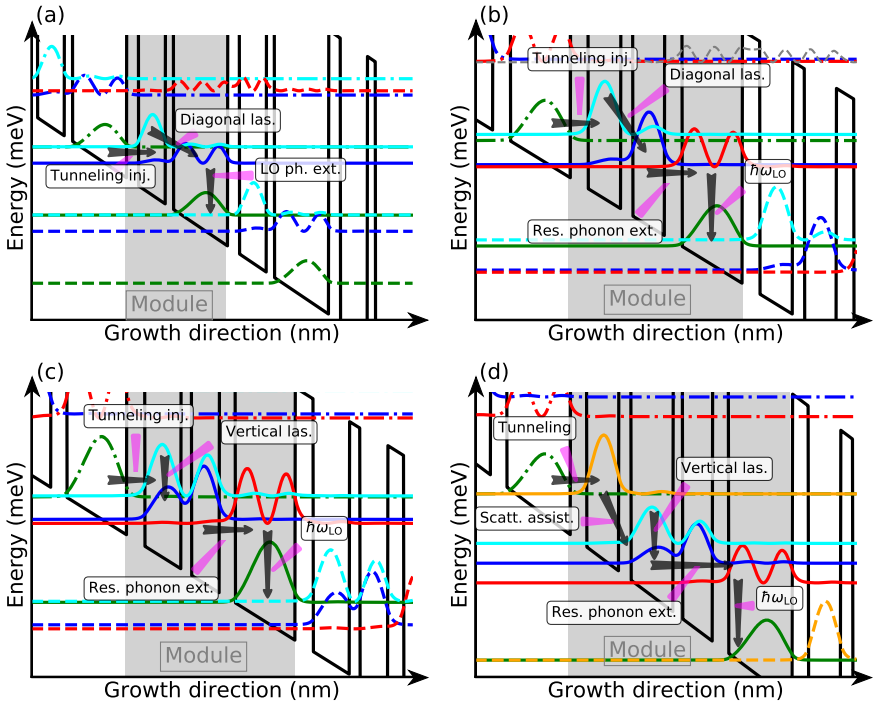

Figure 1.4: Illustration of conduction bands for four different THz QCLs with EZ states (see Sec. 2.1.1). (a) LU2022 device studied in Paper II. (b) V812 device studied in Paper I. (c) The device studied in Ref. [24] and also in Chap. 5 labelled as ChassagneuxIEEE2012. (d) The device studied in Ref. [25]. Arrows show the injection, lasing and extraction mechanisms. The extensions of the single modules are displayed by the gray areas.

via LO phonon scattering to the injection level. This mechanism is called resonant phonon (RP) extraction scheme[23].

Fig. 1.4(a) shows the direct LO phonon extraction where the lower laser level is aligned vertically with the injection level. This is usually the case in two-well designs due to their simple and compact structure involves only three levels, the injector, the upper and the lower laser levels. RP extraction mechanism on the other hand is shown in panels (b), (c) and (d) where additional extraction barriers are introduced and the lower level is depopulated by the resonant tunnelling to the extraction level before the LO phonon transition to the injection level.

Lasing transitions

With achieving enough inversion, the lasing transition occurs between the upper and the lower laser levels. This lasing transition is done either vertically or diagonal in case of the existence of a lasing barrier between the laser levels.

Fig. 1.4(c) and (d) show the scenario of vertical lasing transitions. Here, the upper laser level is aligned vertically above the lower laser level in the same well. In panels (a) and (b) this transition rather arises diagonal. Increasing the diagonality (i. e. increasing horizontal distance between the upper laser level and the injection level) is usually desired to prevent scattering from the upper laser level to the lower laser level or the injection level of the subsequent module. Therefore, it is common to see QCL designs with diagonal lasing transitions to provide sufficient inversion.

Injection Schemes

The population in the upper laser level is achieved by injecting the carriers from the injection level. The most common injection scheme is the tunneling injection. This is the mechanism when the injection and the upper laser levels align and due to their resonance, the carriers are transported to the upper laser level, creating the inversion. This injection scheme is shown in Fig. 1.4(a), (b) and (c) where the injection and the upper laser levels align.

Another option is to use the scattering assisted (SA) injection. This is the process of resonance tunneling of the carriers from injection to another level in the neighbouring well. Here, due to the energy separation between this additional level and the upper laser level is close to the LO phonon energy, LO phonons scatter to the upper laser level and create inversion. This mechanism is shown in Fig. 1.4(d) where the upper laser level is populated by the LO phonon scattering. However, these designs are not very common. This might be due to the long module length providing less gain per length and their more complicated structure results in scattering of the carriers between the levels thus reduces the inversion.

1.3 Negative Differential Conductivity

Achieving a proper emission of light in a QCL design is depending on few key points. First, sufficient population inversion needs to be established. Secondly, the gain must match and overcome the wave guide and mirror losses. Finally, the electrical stability of the design at the operation point is desired [16]. Here,

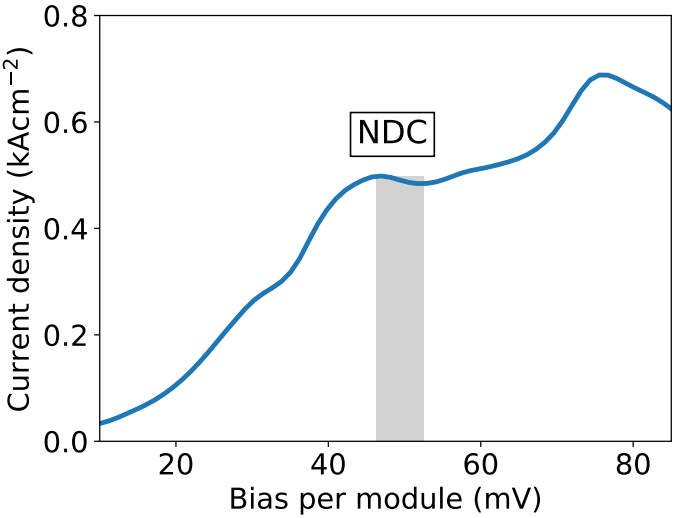

Figure 1.5: Simulated non-lasing current bias relation for the device studied in Ref. [26]. The appearance of the NDC region is highlighted by the gray area.

we briefly mention about the appearance of the negative differential conductivity (NDC) region in the current-bias relation which results in instabilities at the operation point.

The resonant tunneling due to the alignment of the levels provides current flow inside the modules. As the applied bias increases, resonances between the higher states become relevant and they contribute more to the overall current density. Usually, a stable operation point is achieved around the maximum current. This is not the case for devices with NDC. Here, presence of the NDC region implies a drop in the current densities with increasing the bias. This forms a characteristic N-shape behaviour in the current-bias relation and two separate current peaks occur [27].

Such scenario is shown for a THz QCL device in Fig. 1.5 where the data is obtained by our non-equilibrium Green's functions (NEGF) package discussed in Chap.2. Note that, the results are shown here are without the irradiation (no ac field is applied). Here, due to the detuning of the levels with increasing field, current drops after the resonance following the first current peak at 46 mV. At higher bias, alignment with the higher states become relevant and the current increases again resulting a second peak at 75 mV. Here the appearance of the N-shape region

becomes clear and the NDC region is highlighted between 46 and 52 mV.

Following the decrease in current after the first current peak, the electric field distribution becomes no more homogeneous and forms domains instead [28]. This causes instabilities and usually prevents stable operation points. In Chap. 3, we focus on the formation of these electric field domains for extended THz QCLs with NDC and introduce our domain model to analyse the dynamical evolution of the electric field distributions.

1.4 Motivation of this thesis

Quantum cascade lasers are now one of the few sources to generate light in far to mid infrared region. However, there are still issues and improvements needed to be studied to improve their quality and applications. For THz QCL, the main issue is the achievement of operation at the room temperature. Here, any improvement in the maximal operation temperature reduces the need of cooling and is of highest relevance for the technical realization. Another one are the electrical instabilities in the appearance of NDC. In this work, we provide background information of the Papers which focuses on such issues and suggest improvements in the field. The source of our simulations are based on our Non-equilibrium Green's function (NEGF) model and the computational scheme with necessary inputs is explained in Chap. 2.

The motivation of this thesis is based on three aspects. First aspect is the study of the electric field domain dynamics for devices with negative differential conductivity (NDC). Since the appearance of an NDC results instabilities at the nominal operation point (NOP), our inhomogeneous domain model studied in Chap. 3 provides understanding of the electric field distribution inside the modules. Corresponding work is done in Paper III where we investigated the spectral behaviour of the light and its dependence on the initial and the boundary parameters.

Second aspect is the study of chaos theory in THz QCLs. This idea was implied after observing irregular voltage oscillations for the device studied in Ref. [18]. These complex oscillations are studied in Paper I and we show the first autonomous THz QCL exhibiting chaos. This is quite exciting since autonomous time dependent chaotic systems are quite rare and the chaotic signals can be applied for secured communication systems [29].

Third aspect is the study of high temperature performances of THz QCLs. This

study is done in Paper II where we provide a two-well design operating at the highest temperature of 265 K around 4 THz. Further unpublished results are shown in Chap. 5 where we expand our investigation on low frequency designs around 2 THz. Here, we show a trend of simulated phonon and experimental heat-sink temperature difference directly proportional to the maximum currents. Also, based on the device studied in Paper II, we suggest two-well designs with operation temperatures higher than 200 K around. This is an ongoing work and aimed to enable technological applications of QCLs operating around 2 THz with thermoelectrical cooling.

Chapter 2

The Model

In this chapter, we show a brief theoretical background of THz QCLs and the computational flow which we used to simulate the corresponding devices. The chapter is divided into two parts: First, we define the general Hamiltonian for the related QCL systems where the eigenstates are used for the calculations and the description of basic phenomena. Secondly, we show the simulation scheme and the corresponding input parameters of the NEGF package we used the extract quantitative results to analyse temperature performances in Paper II and Chap. 5. Further details can be found in Refs. [30, 28, 31, 32].

2.1 General Hamiltonian

To start with, the time dependent Hamiltonian of the system reads

$$H(t) = H_0 + H_{\mathrm{DC}} + H_{\mathrm{scatt}} + H_{\mathrm{AC}}(t) \tag{2.1}$$

Here, the first term H_0 is the kinetic energy of the free particle and the potential of the heterostructure without an applied bias. The second term includes the applied DC voltage via the potential $-eFz$ where the z-direction is the growth direction of the layered structure and F is the electric field. Knowing the charge distribution we add the mean field part in this term. Albeit implemented, the mean field does not provide a significant difference for THz QCLs studied here due to the short lengths. Both H_0 and H_{DC} are diagonal in the momentum space

k describing the behaviour parallel to the layers. The third term includes all the non-diagonal elements in k regarding to the scattering mechanism and solving this part with the NEGF package provides the kinetics. The final term, $H_{\mathrm{AC}}(t)$, adds the AC field (and the dynamical mean field). Solving the AC part with the NEGF package provides the photo-assisted current describing the gain. In the model, the applied laser field is defined as the classical electromagnetic field in Lorenz gauge $-eF_{\mathrm{ac}}z\cos\omega t$ [31].

There are few more approaches to solve the kinetics of the charge carriers such as rate equations [16, 33] and Fermi-Golden rule [34, 35, 36] or Monte Carlo simulations [37, 38]. Introducing the density matrix allows us to describe the coherencies which are in particular relevant for the tunneling injection [39]. The density matrix is not a quantity to be calculated easily when the order of the energies are comparable for the electron scattering, tunneling and the emitted light. In our NEGF model, the treatment to the density matrix is done by lesser Green's functions

$$\rho_{ij} = \frac{1}{2i\pi}\int_{-\infty}^{+\infty} dE\, G^{<}_{ij}(E,k) \tag{2.2}$$

From the density matrix we evaluate all the observables such as the current densities in a straight forward matter [31].

2.1.1 Choices of basis

We describe electrons in the conduction band of semiconductors via the common envelope function approach [40] where the microscopic lattice structure is reflected by the band edge E_c of the conduction band and the effective mass m_c at the gamma point. Specifically, we use the two band approach which includes non-parabolicity [41, 16, 42]. On this basis, H_0 is determined from the specific layer structure of the QCL studied here. In the following, all wave functions are actually envelope functions. The current is calculated within this two band model following Ref. [32].

As QCLs consist of periodic repetitions of the central module, eigenfunctions of H_0 are Bloch functions with band index ν. For each band we can construct Wannier functions localised in a single module [43]. These Wannier functions are periodically repeated for each module and have the same expectation value of the

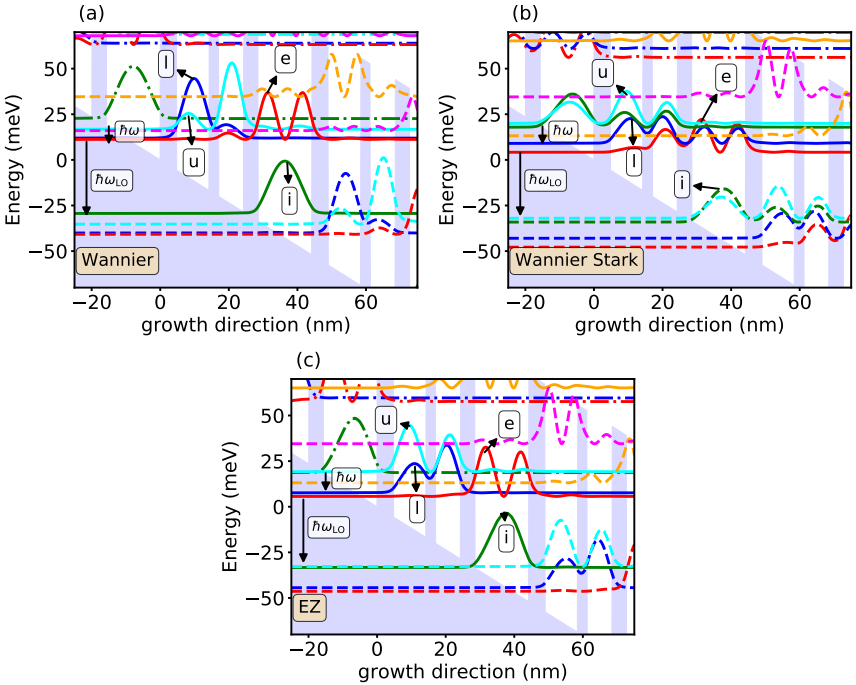

Figure 2.1: Illustrations of a three well THz QCL design studied in [24] with applied biases of 52 mV. Wannier states in (a), Wannier Stark states in (b) and EZ states in (c) are used to visualise the electronic states in the heterostructure. Design includes upper (u), lower (l), injection (i) and extraction (e) states as well as parasitic states in higher energies. The lasing transition and the LO phonon extraction energies is highlighted by arrows on the left side of the panels.

energy as given by the center of the Bloch band they originated from. These Wannier states for different bands ν and/or localised in different modules form an orthonormal basis for the Hilbert space. By restricting the number of bands of the Bloch states we limit the basis up to a certain energy cutoff. Within this basis all further calculations are done where we routinely check that the cutoff is sufficiently large for not changing the results. These considerations refers to the z-direction of the heterostructure. In addition, the lateral degrees of freedom $(x, y = \mathbf{r})$ are taken into account by plane waves $e^{i\mathbf{k}\cdot\mathbf{r}}$.

The Wannier-Stark states are defined as the eigenstates of $H_0 + H_{\mathrm{DC}}$ where an applied voltage is taken into account. These states are periodic upon shifting the

energy by eFd where d is the length of the module. They provide the best estimate for the energy levels. Also, their energy difference can be used to estimate the lasing frequencies. Therefore, in the heterostructures studied in Chap. 5 we use Wannier-Stark (WS) states for illustrative purposes.

Recently in paper II, we also introduced a new set of states with the combination of energy selectivity and spatial localization which we call EZ states. These states are introduced when the energy differences between several WS states are less than the broadening. This set of states we refer as a multiplet. The EZ states are the linear combinations of the states in the multiplet which diagonalises the z-matrix. These new states have roughly the same energies as the multiplet states. The Hamiltonian exhibits non-diagonal elements between different states resulting from the multiplet, which are the mutual tunnel matrix elements. In the following simulations we usually choose the energy separation of less than ≈ 5 meV to introduce these multiplets.

Here in Fig. 2.1, the differences between Wannier-Stark, Wannier and EZ states are shown for a three well THz design studied in Ref. [24]. In both panels the injector, the upper laser, the lower laser and the extraction states are included as well as the higher parasitic states. The lasing transition from upper to lower level as well as the depopulation of the extraction level by longitudinal optical (LO) phonon transitions ($\hbar\omega_{\mathrm{LO}}$) are highlighted by the black arrows. In each panel, phonon temperature is fixed to 150 K and 52 mV per module is chosen at the peak currents. Here, the Wannier-Stark picture in panel (b) clearly reveals the resonance between the injection and the upper laser state. As the presence of the applied DC voltage shifts the states, the energies become aligned. This is not the case in (a) where Wannier states are used to illustrate the occupations. Since the Wannier states are defined without any applied bias, a slight shift in the energies are observed in the absence of bias. Therefore, they are not suitable to follow the correct energy values of the levels and the energy of the lasing transitions. Following the small energy separation between the injector and the upper levels in Wannier Stark picture, we show the EZ states in panel (c). Here, the EZ states provide an even more clear distribution of the ground and the upper laser levels.

2.2 Computational scheme of the NEGF package

The NEGF model is used by various groups [44, 45, 46] to solve the kinetics of the charge carriers in the QCLs. In this section, we show the simulation scheme

and the inputs necessary to simulate our NEGF package which is used to extract quantitative results of THz QCLs studied in this thesis and the corresponding Papers.

Before simulating the NEGF program, we first need to calculate the Wannier states since they are used as the corresponding basis. To calculate the Wannier states, we need the following parameters:

- Layer sequences.
- Effective masses.
- Conduction band offsets at the Gamma point.
- The Kane parameter applicable for the heterostructure system used.

With entering these parameters, our Wannier program produces data of the Wannier states and creates input files to use in our NEGF program. Here, we can make a simple illustration of the related heterostructure with the Wannier states under zero voltage or with the Wannier-Stark states with entering applied bias but without considering the mean fields.

Following the generation of the Wannier data, we now prepare to start our NEGF program. To do that, we first need the physical parameters as doping profile, interface roughness parameters, material parameters for phonon scattering and material parameters for alloy scattering. We also introduce the phonon temperature which determines the occupation of the phonon modes.

Inside the input file, we vary the parameters such as the number of neighbouring periods N_{per}, the number of Wannier states per period N_{nu}, the number of harmonics N_{h}, the range of applied DC voltage eFd, the frequency range ω, the range of applied AC field $eF_{\mathrm{ac}}d$ and the waveguide and mirror losses. Here, the total number of the states are calculated via $N = N_{\mathrm{nu}}(1 + 2N_{\mathrm{per}})$ following Ref. [32].

With gathering all the necessary input information, now we start the NEGF program. The flow of the computation is shown in the following order:

- Initial guess of the self energies.
- Calculation of the energy dependent Green's functions
- Calculation of the current and densities.

- Calculating and updating the mean field, and the new self energies from the Green's functions.
- If converged, move to the next F_{dc} for non-lasing case, for gain move to the next ω and for lasing case move to the next F_{ac}. If no convergence, repeat the process from step two.

Even though the NEGF approach provides consistent results [32, 30, 31],the computational process is quite slow and based on many self consistent iterations. Here, the main idea is to accomplish the convergence quickly. In the simulations, we accept a good convergence is achieved when the old self-energies differ from the new ones by less than $2 * 10^{-4}$.

To calculate non-lasing currents, we only apply dc field eFd without harmonics. To calculate the linear gain, we apply a small AC field strength $eF_{\mathrm{ac}d}$ (usually between 0.1 and 1 meV) and increase the number of harmonics $N_h = 1$ either for the selected bias point or in a bias range of interest with varying eFd. To calculate the lasing currents (and non-linear gain), we increase the AC field strength higher and depending on the convergence, we might need to use higher harmonics. We usually avoid using higher harmonics since the time of the computational process increases proportional to the N_h. Eventually, if the iterations converge, we extract the current, the gain and the density data for the related heterostructure.

The results of our NEGF package is used to calculate homogeneous current densities and gains in Paper I, Paper III and Chap. 3 as the input of our inhomogeneous domain model. In Paper II we use the NEGF program to study higher temperature performance of two-well QCLs operating around 4 THz. Typical results are shown in Chap. 5 where we use the NEGF package to study temperature performance of QCLs operating around 2 THz. We also include new data on our ongoing project where we suggest designs promising the highest operation temperatures around 2 THz based on the two-well structures studied in Paper II.

2.2.1 Resolved Visualization of Current and Electron Densities

Following Eq. 2.2, we use lesser Green's functions $G^<$ to solve the density matrix and the current densities. Here $G^<$ provides information on energy. This allows us to compute energetically and spatially resolved current and particle densities. Fig. 2.2 shows the resolved current and particle densities for a four-well design studied in Ref. [26]. In panel (a) the spatial extension of the current density through the barriers are clearly seen. Due to the alignment of the higher

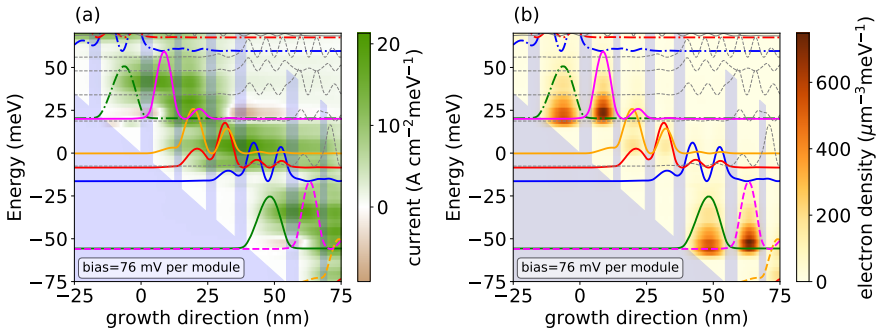

Figure 2.2: Energetically and spatially resolved current and particle densities in (a) and (b) extracted from NEGF package respectively. The device shown here is studied in Ref. [26] at 76 mV bias per module and phonon temperature of 150 K. EZ states are used to visualise electronic states. The conduction band offset of $0.831x$ eV is used in the simulations.

states, this current extension at the edges of the barriers provides information on the leakage current through the parasitic states and to the continuum. In panel (b), location of the particle densities are shown by resolved densities. This also enable us to observe the location of the inversion as the majority of the particles are localised in the upper state as well as very few population in the lower level.

In the Chap. 5 and Paper II, we use the resolved plots to analyse the quality of the designs and the temperature performances of THz QCLs. The resolved current plots allow us to track the undesired currents due to the thermally activated scatterings. The resolved density plots provide the spatial extension of the carriers (especially the density distribution between the injector and upper laser levels) as well as the locations of the absorption between the injection and lower laser states.

Chapter 3

Dynamics of Electric Field Domains

The model used in Chap. 2 implies that the total bias drop is distributed homogeneously over every module. This assumption is based on matching the electron and sheet doping densities in the modules. This is not the case for extended QCLs if they exhibit NDC. The increase in the particle fluctuations shatters the equal distribution of the electron densities in each module. Thus, the electric field distribution becomes unstable and domains form with different electric fields [47, 48, 49, 50]. These electric field domains are observed in both stationary[51, 52, 53] and oscillatory formations [54, 55]. Previously, unstable field distributions were known to prevent stable operation points inside the NDC region and were usually preferred to be avoided. Recently, it was shown that the stable operation point is possible inside the NDC by the ignition of the lasing fields in the presence of the oscillating electric field domains [18].

In this chapter, we describe our inhomogeneous field domain model for THz QCLs studied in Paper I and Paper III. We also show the applications of the domain model including the study of the spectral properties of lasing field and the voltage characteristics under various initial and boundary conditions. General methods to solve gain mediums in two level systems as well as the input we used based on fitting the homogeneous gain and current densities are presented in Appendix A.

3.1 Travelling Electric Field Domains

The formation of electric field domains was observed previously such as in Gunn diode due to the self sustained current oscillations inside the NDC region [48, 56, 57]. Stationary field formations and saw tooth behaviour of the current densities are also commonly observed [58, 59, 60, 61]. Thus, different designs have different characteristics of the current - bias relation and consequently different field formations inside the modules [62, 63, 64]. In this section, we show the background theory of our domain model for two THz QCLs V812 (Paper I) and EV2244 (Paper III). The dynamics of the model includes the self sustained iterations of the electric fields, the current densities and the electron densities for each module.

The study of our domain model in this section is based on the dynamical evolution of the electric field domains. Here, the interface between the spatial regions with different electric fields is called a front. This contains a charge (i. e. existence of more or less carriers than the doping) and depending on whether the field is increasing or decreasing, the charge can be positive or negative. The transition from low field to high field requires a negative charge. This attributes to the accumulation front. On the other hand, the transition from high field to low field requires positive charge i. e. depletion front. For highly doped systems, these fronts can be stationary. This is due to the relative increase in the electrons is not too large and they are trapped in a certain module. For a low or medium doped systems, we need a higher excess charge and this is not consistent with trapping the electrons. If these fronts move in time, they are called travelling fronts [28].

To begin with, we introduce the inhomogeneous field distribution inside the heterostructure illustratively shown by the periodically repeated one-well heterostructure as displayed in Fig. 3.1. Here, we treat the excess charges as an average inside the modules. The curvature observed as the charging effects of the electron densities and doping (usually located in the widest well as explained in Paper III) changes the heterostructure potential. Here in Fig. 3.1, the first approximation is that the carriers are localized in the widest well due to the weakly coupling of the quantum wells. The current flow between the modules i and i+1 is labeled as $J_{i\rightarrow i+1}$ and is a function of average field drop F_i and the sheet electron density n_i. For a simplified heterostructure with N quantum wells and $N+1$ barriers, we introduce modified continuity and Poisson's equations to calculate the dynamics of the electron densities and the electric fields [28, 65].

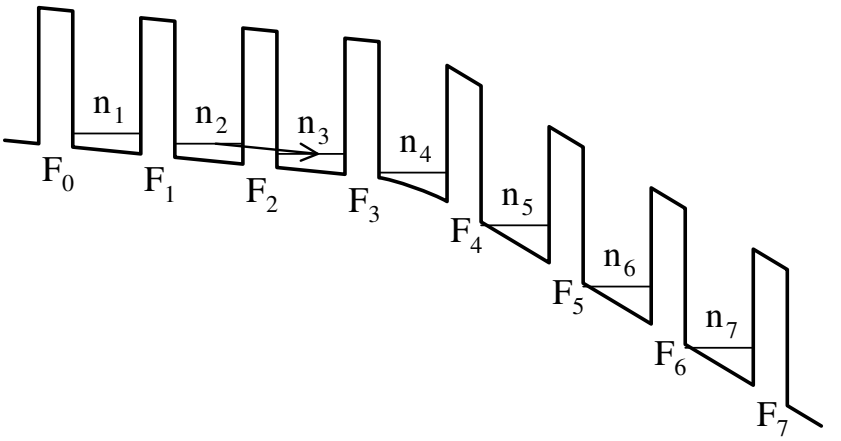

Figure 3.1: Illustration of a one well heterostructure with inhomogeneous field distribution adapted from Fig.22 of Ref. [28]

$$\begin{aligned} e\frac{dn_i}{dt} &= J_{i-1\to i} - J_{i\to i+1} \\ (F_i - F_{i-1}) &= \frac{e}{\epsilon_0\epsilon_r}(n_i - n_D) \end{aligned} \tag{3.1}$$

where $i = 1, ..., N$, n_D is the doping density per unit area and ϵ_0 and ϵ_r are the relative and the dielectric permittivities. In addition, the boundary currents between the injection and receiving contacts are calculated with a phenomenological ohmic conductivity σ relation:

$$\begin{aligned} J_{0\to 1} &= \sigma F_0 \\ J_{N\to N+1} &= \sigma F_N \frac{n_N}{n_D} \end{aligned} \tag{3.2}$$

The effects of the boundary conductivity was recently shown as crucial on field dynamics [65] especially in systems with relatively low doping where the travelling fronts oscillate as studied in Paper III.

By applying the time derivative to the Poisson's equation in Eq. 3.1, combination with the continuity equation provides the dynamics of the local fields evolve with the total current density $J(t)$ and the current flow from module i to i+1 $J_{i\to i+1}$

$$\frac{dF_i}{dt} = \frac{1}{\epsilon_0 \epsilon_r}(J(t) - J_{i\to i+1}) \tag{3.3}$$

The QCL voltage is also defined as the sum of the fields over the modules with module length of d as

$$U_{QCL}(t) = \sum_{i=0}^{N} F_i(t) d \tag{3.4}$$

The total current density can be extracted with inserting Eq. 3.4

$$J(t) = \frac{1}{N+1}\left(\frac{\epsilon_0 \epsilon_r}{d}\frac{dU_{QCL(t)}}{dt} + \sum_{k=0}^{N} J_{i\to i+1}\right) \tag{3.5}$$

In our model, the current in each module is calculated by the average electric fields between the electron densities in neighbouring modules. Also, the homogeneous current density is calculated by fitting $J(F_{\mathrm{dc}}, F_{\mathrm{ac}}, \omega)$ which is extracted from the NEGF package as defined in Eq. A.9. Here, we accept that the doping density and the carrier densities differ from each other. Thus, following Refs. [18, 28, 50, 52] the current density inside the modules can be written as

$$J_{i\to i+1} = J(F_{\mathrm{dc}}, F_{\mathrm{ac}}, \omega)\frac{n_i - n_{i+1}F(F_i, T)}{n_D - n_D F(F_i, T)} \tag{3.6}$$

Here, we assume that the current density is proportional to the electron density in the module i. This current is decreased by the thermally activated backward currents in the neighbouring modules i+1 with proportional to the function $F(F_i, T) = e^{-eF_i d/k_B T}$. In addition, the doping density normalizes Eq. 3.6 and the homogeneous current is recovered when electron densities in modules i and i+1 matches with the doping density [65].

The total current density J(t) is usually calculated when an external circuit is introduced. In Paper I and Paper III we consider the total current calculated via Eq. 3.7 for the external circuit shown in Fig.3.2. The circuit includes a parallel capacitance C_p, load and probe resistances R_L and R_p and the Schottky potential V_B to align the conduction band at the metal contact.

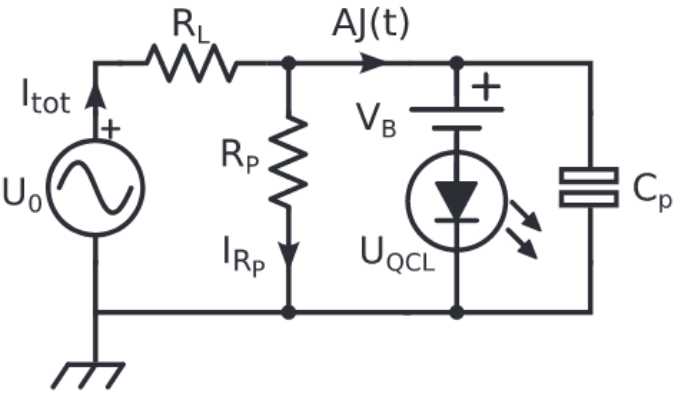

Figure 3.2: External Circuit design used to simulate V812 and EV2244 taken from Paper I and Paper III.

$$AJ(t) = \frac{U_0 - U_{\mathrm{QCL}}(t) - V_B}{R_L} - \frac{U_{\mathrm{QCL}}(t) + V_B}{R_p} \tag{3.7}$$

In the following sections, we use Eq. 3.7 to calculate the total current for both V812 and EV2244 designs. The $J(t)$-U_{QCL} relation is called load line and determines the stationary point. The related operation points are highlighted by the load lines in Fig. 3.5 with gray straight lines representing the external voltage U_0.

3.1.1 Applications of the domain model

The dynamical equations of the electric fields with our inhomogeneous field distribution is defined in the previous section. In this section, we show the simulations of the time evolution of the self-sustained bias oscillations and the travelling electric field domains for the devices V812 and EV2244. The model provides the electric field distribution and the carrier motion in the modules as a function of time.

For the devices studied here, we usually observe a low field at the injection and high field at the receiving contact. Fig. 3.3 shows such a scenario of the electric field distribution as a function of time and module index. Here module index 1 represents the injection contact and N'th (222 for V812 and 151 for EV2244) represents the receiving contact. It is clear that for a given time t, the electric field

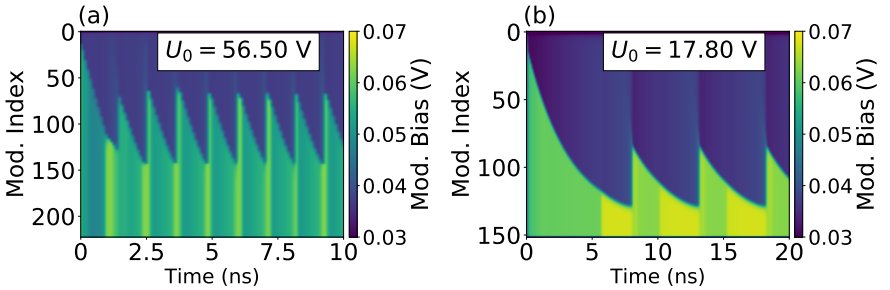

Figure 3.3: Travelling electric field domains as a function of time and module index for two devices V812 in (a) and EV2244 in (b). The operation points U_0 are shown in the white boxes. Here the boundary conductivities at the contacts are $\sigma = 0.15$ A/Vcm in each panel.

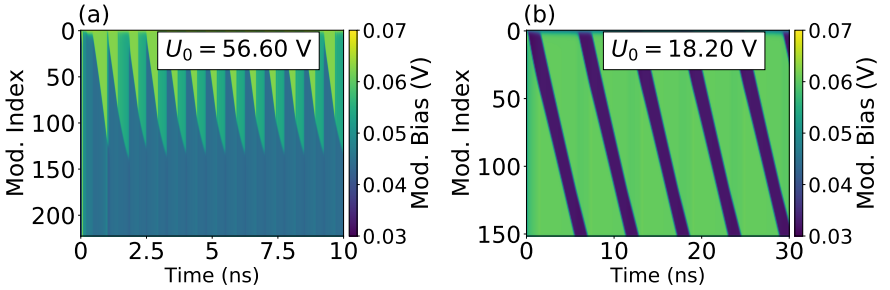

Figure 3.4: Travelling electric field domains as a function of and module index for the devices V812 in (a) and EV2244 in (b). Here the conductivities at the contacts $\sigma = 0.05$ A/Vcm in (a) and $\sigma = 0.03$ A/Vcm in (b).

is distributed differently inside the modules with the low field dominating the injection contact. This is the case of accumulations fronts as discussed previously. With iterating time, the field domains moves back and forth between the contacts due to change in field distributions inside the modules. Following the decrease in the spatial extend of the high field domains e. g. at $t = 13$ in (b), due to the instabilities, new domains form. This formation of the new domains reveals an oscillatory behaviour and the oscillation frequencies are depending on the velocity of the fronts [28].

In addition to the accumulation fronts, there are also depletion fronts regarding the positive charges. These are usually faster due to lesser electrons [28]. The

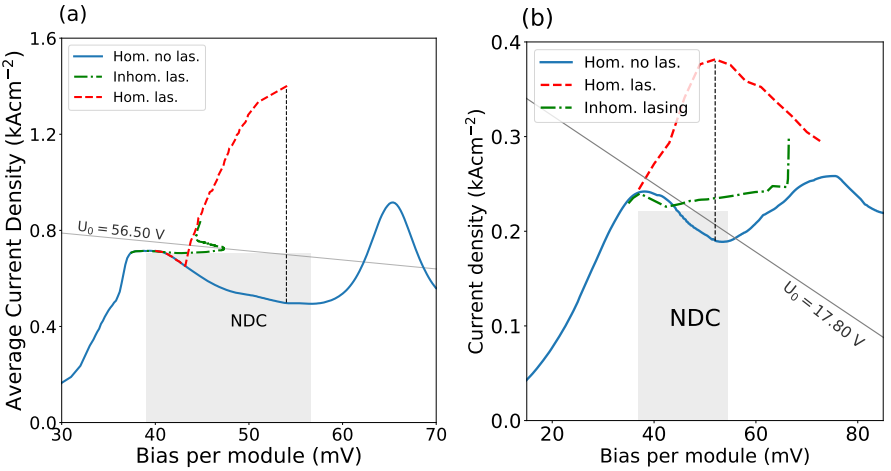

Figure 3.5: Current-bias relation with and without irradiation for devices V812 and EV2244 shown in Fig. A.2. Additionally, average current is extracted from inhomogeneous domain model in shown with dashed dotted curves. Gray lines represent the load lines.

presence of the depletion fronts is usually observed when the high field domains form around the injection contact as seen in both panels of Fig. 3.4. This scenario is usually observed when the phenomenological boundary conductivity is relevant as studied in Paper III and in Eq. 3.2. As the boundary current drops inside the NDC, we observe (when σ is lower) that the high fields shift to the injection contact and the depletion fronts become relevant due to the requirement of a positive charge.

The spatio-temporal time averages of the current densities from the domain calculations are shown for V812 and EV2244 by dash-dotted curves in Fig. 3.5. Here, the solid and dashed curves are the homogeneous lasing and non-lasing current densities extracted from the NEGF package. The load currents are shown by the gray lines with the respective operation points $U_0 = 56.50$ V in (a) and $U_0 = 17.80$ V in (b). These operation points are used in Fig. 3.6 where we show the QCL bias U_{qcl} calculated by the sum of the electric fields following Eq. 3.4 as a function of time. It is observed that the frequency of the bias oscillations are quite large in V812 in (a) compared to EV2244 in (b). The frequencies of the oscillations are ≈ 800 MHz in (a) and ≈ 150 MHz in (b). Also, the amplitude of the oscillations vary by 2 V in (a) and 0.6 V in (b). In addition, in Paper I

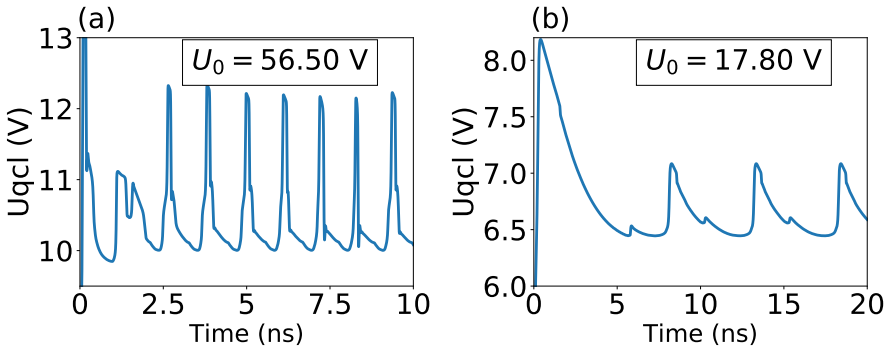

Figure 3.6: Average QCL voltage for all modules as a function of time for two devices V812 in (a) and EV2244 in (b). The external applied voltages are highlighted by the boxes in top center.

the irregular oscillations shown in (a) are taken into account and chaos is studied. This is not the case in (b) where the bias oscillations are quite regular.

3.1.2 Analysing of the lasing field

In this section we study the spectral behaviours of the lasing field as discussed in Paper III with introducing the photon numbers in the Fabry-Perot cavity modes. For each mode "j" the average photon number N_j^{ph} is related with the ac field strength F_{ac}^2 with a single frequency ω_j. The gain of each mode is averaged for all modules and calculated from the fitted gain shown in Eq.A.6

$$G(\omega) = \frac{1}{N n_D} \sum_{m}^{N} n_m \frac{G_0(\omega)}{1 + \tau\gamma(\omega_j^{'})F_{ac}^2} \tag{3.8}$$

with the life times of the upper laser states τ. Here, the probe frequency ω is separated from the frequency of the ac field $\omega^{'}$. This provides us to study the saturated gain with selected frequencies. This is not the case in NEGF package where a single frequency is provided. Also, we assume that the gain is a function of the electron density n_m in the modules. Each cavity mode "j" contributes to the gain saturation in every module "m" with a gain recovery time which is usually around 1 ps or less following the Ref. [18]. The photon life time is assumed to be around 5-6 ps, thus the gain can be written as a direct function of the field

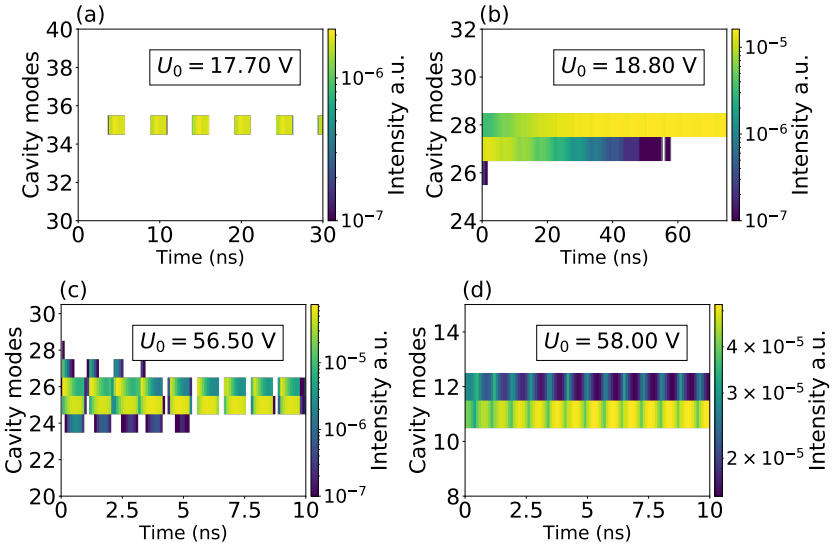

Figure 3.7: Lasing intensity as a function of time and cavity modes for different operation points. In (a) and (b) simulations for EV2244 are shown as well as V812 in (c) and (d). To reference, cavity modes 25, 30 and 35 are equal to 3.57, 3,71 and 3,85 THz in EV2244 and cavity modes 10, 20 and 30 are 2.77, 3.17 and 3.57 THz for V812 respectively. Contact conductivity is taken as $\sigma = 0.15$ AVcm^{-1} in each panels.

intensity. Following the chapter 7 in Ref. [16] and Ref. [18] we can write the photon numbers in the cavity mode "j" as

$$\frac{dN_j^{ph}(t)}{dt} = \frac{c}{n_g}(G(\omega) - g_{loss})N_j^{ph}(t) + I_{sp}^j \tag{3.9}$$

where

$$I_{sp} = \sum_m^N \frac{An_m^U}{\tau_j^{sp}} \tag{3.10}$$

Here $n_g = 3.6$ is the group refractive index, τ^{sp} is the spontaneous emission of light from upper laser state[66] and taken as 3 ms in the simulations (see the

discussion in Ref. [18]), g_{loss} contains the waveguide and mirror losses and c is the speed of light. Following the approximations in Ref. [67], for devices V812 and EV2244 operating above 3 THz, the losses are approximated by $g_{\text{loss}} = 20$ cm^{-1}.

Fig. 3.7 shows the lasing fields in the cavity modes as a function of time for devices EV2244 and V812. In the horizontal panels, we show the lasing fields by two different external voltages for the same device. As the spatial extend of the high fields grow with time, the gain matches with losses and lasing switches on (see between 8 and 10 ns in Fig. 3.3(b) and Fig. 3.7(a) for EV2244). This usually exhibits lasing in higher frequencies. With a sufficient increase in the current while entering the high field domain, current matches with the low field domain and results lasing in the low frequency range (see between 4 and 4.6 ns in Fig. 3.3(a) and Fig. 3.7(c)). Increasing the external bias stabilizes the lasing field and continuous lasing persists as seen in mode 28 in panel (b) and 11 in (d). As the front velocities are relatively slower in EV2244 as seen in Fig. 3.3(a), there is a longer time period between each pulsation of the lasing field. The rapid pulsations in V812 are due to the much higher velocity of the travelling fronts between the high and low field domains as seen in Fig.3.3(a).

In extended QCL devices with NDC, the field domain model provides a comprehensive analysis of the dynamical evolution of the systems. In addition, the characteristics of the QCL voltage and the spectral properties of the lasing field depends on the boundary and initial conditions. Such calculations and analysis are done in paper I and III. In paper I, we mostly focused on the irregular voltage oscillations and provided rigorous analysis for chaos theory. In paper III, we show how the spectral properties are sensitive to the contact conductivity and the parallel capacitance connected to the external circuit.

Chapter 4

Chaos

Chaotic systems usually exhibit random and complex behaviours in the long time limit. Typically, noise is not of relevance and the study of such systems is also referred as "deterministic chaos" [68]. Modelling such systems is quite hard since they become unpredictable in longer time periods. There are few concepts to observe such systems; the accuracy of the measurement, well defined time scale and acceptable amount of uncertainty during the observations. One main concept is the definition of a reasonable time scale where the model turns from easily predictable to complete random. The time scale for these systems is called Lyapunov timescale [69, 70]. This could be days for a weather forecast or millions of years for an orbital system. In such systems the dynamical evolution becomes exponentially more random and complicated with time, e. g. prediction of the weather forecast become more unreliable for the next four days than two days. Thus the chaos theory is used to model such systems and the theory consists of proper predictions with introducing mathematical models.

There are many approaches to provide understanding of the chaotic systems. One and multi dimensional maps, Fractal geometries, attractors, conservative and dissipative systems are few examples to categorize them under common mathematical models. Following Refs. [71, 72], there are a few rules to imply whether a system is chaotic or not. First, the system should be sensitive to its initial conditions which is related with a positive Lyapunov exponent. Second, the phase spaces of the system should overlap thus the topology become mixed. Finally, the periodic orbits of the system should be dense [73]. These fundamental concepts are used to

identify chaotic behaviour in Paper I where we introduced the first autonomous THz QCL exhibiting chaos.

In this chapter, we first study the common logistic map. Here, we show the definition of the stable points and how the iterations evolve with the control parameters. Following, we study bifurcation diagrams, Lyapunov exponent and phase portraits. These models are used as the basis of indications of our chaos study in voltage oscillations of a THz QCL in Paper I. Finally, we show three chaotic examples of autonomous systems without periodic driving; the Lorenz map, the coupled pendulum and the three body model. Here we compare the similarities of the phase portraits with the quantitative results shown in Paper I.

4.1 Modelling Chaos

In this section, we show common approaches to study chaos in non-linear systems. These approaches include the construction of the bifurcation diagrams, phase portraits and Lyapunov exponent. We first introduce the most common logistic map example to provide a brief understanding on the fixed points.

To start with, we introduce a simple example of tracking the population dynamics in a system [74]. Let's assume the number of the population of a system with x (e.g. micro organisms in an environment) and define the time unit by the number of days d. In the simplest model, the organisms reproduce with a rate "r" in every generation. This is shown by the relation

$$x(d+1) = rx(d) \tag{4.1}$$

with a change in the population of each day by $x(d) = r^d x(0)$. Depending on whether r is larger or less than 1, the change in population will either results in an exponential growth or extinction. However, they would not grow infinitely due to the limited environment (e. g. lack of food and nutrition). Therefore, we introduce a more complex function motivated by the reproduction with extracting some saturation. This function is the "Logistic function" which is one of the most common models to study the conditions and behaviour of the complexity [75, 68] and can be written as

$$f(x) = rx(1-x) \tag{4.2}$$

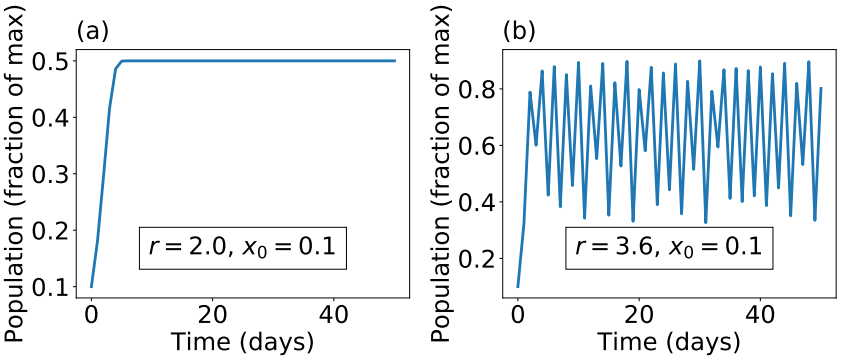

Figure 4.1: Time evolution of the function of logistic map for $r = 2.0$ in (a) and $r = 3.6$ in (b) are shown. The initial points are fixed in each panel as $x_0 = 0.1$

The time iteration of this logistic function is also known as the "Logistic map" and defined as

$$x(d+1) = rx(d)(1 - x(d)) \tag{4.3}$$

Here, the function $f(x)$ is close to rx for small x but is reduced for larger x.

Assuming the initial condition is $x(0)$, each iteration results more and more complicated analytical expressions. Thus a computational analysis is needed. Following the two different control parameters $r = 2.0$ and $r = 3.6$ with the same initial condition $x_0 = 0.1$, time iterations of the logistic maps are shown in Fig. 4.1. Here, we show that the evolution of the function is highly depending on the control parameter. In panel (a), the stabilization of the function occurs within a few days thus the long time estimations of such a distribution is possible. In panel (b) on the other hand, quite complex oscillations occur and prevent consistent estimations.

Assuming some long iterations labelled by i of a function $x(i)$ converges to a single point x_c, means that the $x(i)$ and $x(i \pm 1)$ are close to each other for adjacent iterations. Then, we can write the logistic map $f(x)$ at the x_c as

$$x_c = f(x_c) \tag{4.4}$$

Here, x_c is called a fixed point and is usually extracted by the intersection of the

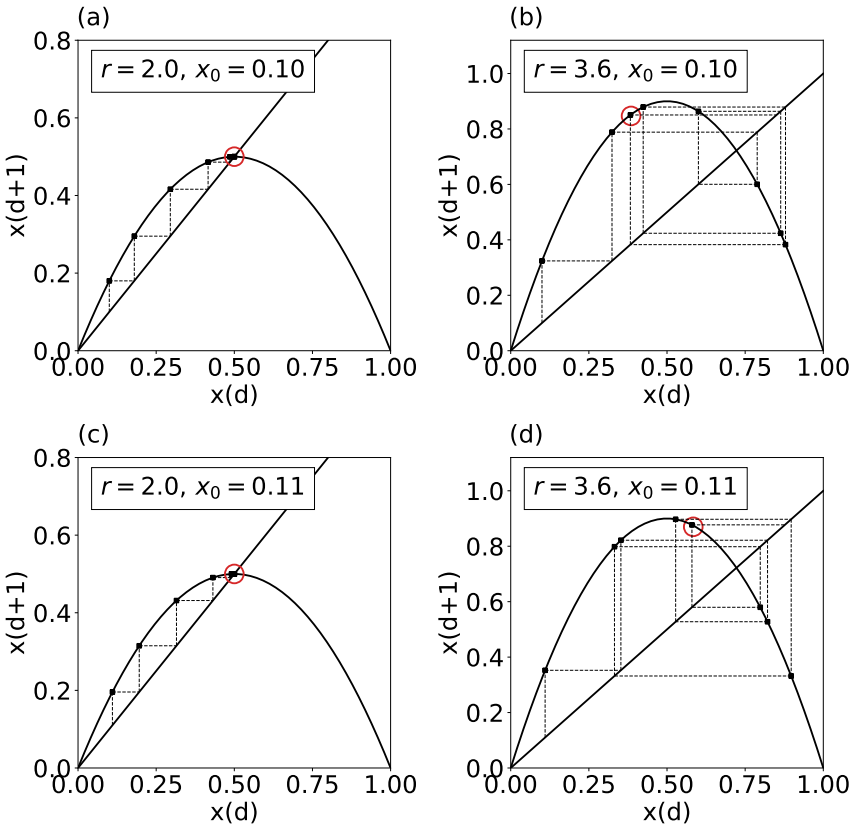

Figure 4.2: Graphical visualization of the iteration scheme of logistic map for varying control parameter r and initial point x_0 are shown. Final iteration points are highlighted by red circles. The figure is inspired from Ref. [74].

function $f(x)$ with $y = x$ curve as seen in Fig. 4.2. Following the figure, we show two scenarios. First, in the horizontal panels two different control parameters are used as $r = 2.0$ in (a,c) and $r = 3.6$ in (b,d) with fixing the initial point x_0. The other scenario is changing x_0 and this is shown by the vertical panels as $x_0 = 0.1$ in (a,b) and $x_0 = 0.11$ in (c,d) with fixed r.

Here in Fig. 4.2, vertical and horizontal dashed lines represent the iterations. This is done by the following logic: starting with the x_0 in the $y = x$ curve, first we draw a line vertically until it intersects with the function $f(x)$. From the intersection point, we continue drawing horizontally until the line reaches $x = y$

curve again. Following the same procedure of drawing vertical and horizontal lines, we follow the sequence of x(d) as given by Eq. 4.3. Sometimes we find convergency to a fixed point (also called an attractor [76]). Here, such convergence is shown in panels (a) and (c) regardless of the choice of initial point. Increasing r provides a different scenario. Here in panels (b) and (d), iterations do not converge to a fixed point rather scatter. This divergence from the intersection usually reveals the existence of an unstable point.

One clear observation here is that in each scenario, independent of the initial condition, the complexity of the system depends mainly on the value of r. However, in case of $r = 3.6$, depending on the initial point, the trajectories of the iterations deviate significantly. This is not the case of $r = 2$ where the iterations eventually converge to a fixed point regardless of the initial condition. This indicates the sensitivity to the initial condition in the complex scenario.

4.1.1 Bifurcations

Previously, we discussed the logistic map as an example of providing the complexity of a system and the fixed point analysis. The bifurcation is the change of fixed points of a system with the control parameter. These fixed points either stay in a stable point or become unstable with varying the control parameter. The case of existence of an unstable point is usually followed by an alternating stable point within a limit cycle which is periodic. Also, bifurcation portraits are used to visualise these fixed points that the system approaches asymptotically as a function of the control parameter. Therefore they provide mathematical expressions based on dividing a system into separate topological solutions.

Bifurcations usually appear in systems defined by non-linear equations [68, 77]. Depending on their dynamical structure, these systems can be expressed by various bifurcation diagrams such as saddle node, trans-critical, sub-critical and supercritical bifurcations [78].

In the top panel of Fig. 4.3, we show an example of a supercritical pitchfork bifurcation of the logistic map. Here, stable fixed points are shown by the straight lines. The points (junctions) where negative Lyapunov exponent goes to zero are the bifurcation points and they are unstable. Following the increase in r after the first bifurcation point at $r = 3$, the pair of two new lines are created. By pair, we mean that the existence of an oscillating new stable point that alternates between these two points (i. e. limit cycle) in time as discussed previously. Increasing r

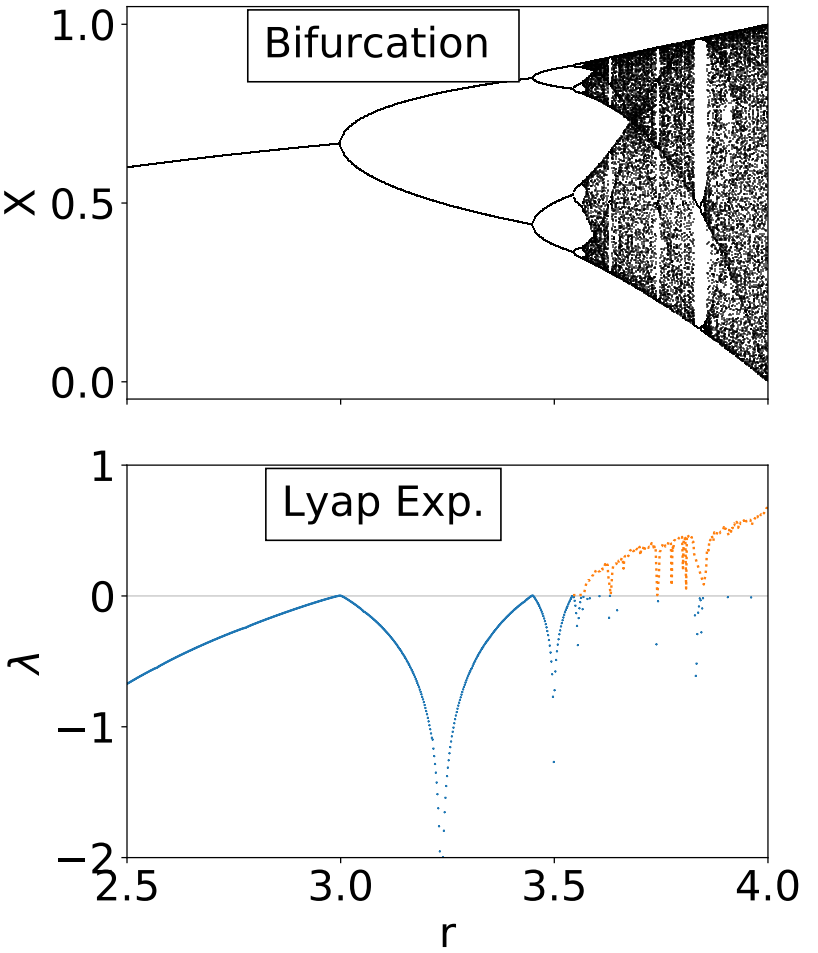

Figure 4.3: Top: The bifurcation diagram for the logistic map is shown. Bottom: respective Lyapunov exponents as a function of control parameter r are shown. The algorithm is adapted from Ref. [79]

further, a new stable point forms following the next bifurcation point and now alternates between four points (see $r = 3.45$). This doubling scenario repeats itself any time the system approaches to a bifurcation point and results in a very dense and complicated structure following $r > 3.6$.

In paper I, we introduce such bifurcation portraits similar in principle with intro-

ducing local minimas and maximas of the QCL voltage oscillations as fixed points. This provided an understanding about the complexity of the system. Note that we use bifurcations as an indication but not as a proof of chaos. The most valid mathematical method to verify chaos is extracting the positive Lyapunov exponents. This is explained in the following section.

4.1.2 Lyapunov exponents

The Lyapunov exponent is a measure of the rate of exponential separations of the adjacent trajectories of a dynamical system. This is done by constructing the phase portrait and tracking the deviation between the neighbouring trajectories. This approach is usually used to understand the sensitivity of the system to its initial conditions and to characterize the chaotic motion (see also the vertical panels in Fig. 4.2) [74, 68, 80]. In this section we provide a brief background on the derivations of the Lyapunov exponents. We also show our approach to process data, following Refs. [81, 82], to extract the largest Lyapunov exponent for a THz QCL studied in Paper I.

Let's assume an infinitesimal non-linear chaotic system with N dimensions slightly perturbed by the initial conditions. As the time iterates until T, the separation of the paths diverges and the distance between them increases as shown in Fig. 4.4. Here, the Lyapunov exponent provide a measure of this divergence between the original and perturbed paths. It is commonly observed that in a chaotic system, this distance grows exponentially as long as the perturbation is not too large [68, 74]. This is because the limitations regarding to the system size. Thus, if we apply a large perturbation, this grow becomes bounded by the size of the system. This exponential growth between the paths are defined by the logarithmic relations we show in the following [74].

Here in Fig. 4.4, two paths with slightly perturbed initial conditions are denoted by $x(i)$ and $x_p(i)$ where p denotes the perturbed path. The perturbed path therefore can be written as

$$\Delta x_p(i) = x(i) + \delta x(i) \tag{4.5}$$

with the amount of infinitesimal deviations from the original path δ. The deviation between the paths with iterations until T increases exponentially as

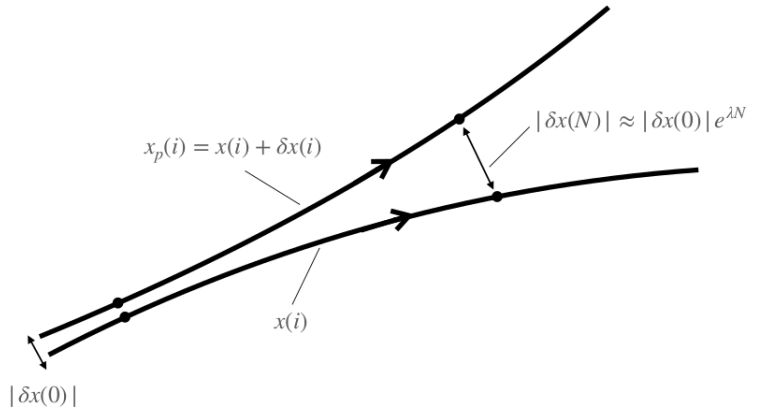

Figure 4.4: Diagram of two adjacent paths of a system with different initial conditions.

$$|\delta x(T)| = |\delta x(0)|e^{\lambda T} \tag{4.6}$$

Here, λ is the Lyapunov exponent and denotes the rate of separation (see Ref. [68]). The exponential term is related with the stretching of the distance between the adjacent points. In the limits of $T \to \infty$ and assuming the $\delta \to 0$, the Lyapunov exponent can be written by a more clear form

$$\lambda = \lim_{T\to\infty} \frac{1}{T} \sum_{i=0}^{T-1} \ln \left| f^{'}(x(i)) \right| \tag{4.7}$$

where

$$\left| f^{'}(x(i)) \right| \approx \left| \frac{\delta x(i+1)}{\delta x(i)} \right| \tag{4.8}$$

Depending on the dimension of the system, there can be also more than one Lyapunov exponent. If the largest exponent satisfies $\lambda_{\mathrm{L}} \leq 0$, the divergence between the two paths either increases slowly or decreases. This will provide sufficient knowledge of the system in longer time periods. However, in case of $\lambda_{\mathrm{L}} > 0$, the divergence between the paths will grow exponentially and predicting the future of

the system becomes unlikely. Thus the construction of the Lyapunov exponent is one of the main mathematical concept of deciding whether the system is chaotic or not.

In the bottom panel of Fig. 4.3 we also show Lyapunov exponents for the logistic map as a function of the control parameter r. To guide the eye, we draw a horizontal line at $\lambda = 0$ and use markers to point the largest Lyapunov exponents. Here, until the system reaches to the first bifurcation point at $r = 3$, Lyapunov exponents are negative. At $r = 3$, Lyapunov exponent approaches to zero, meaning an unstable point forms. The same scenario is shown at $r = 3.45$ where the system approaches to a second bifurcation point. Following the range $r > 3.6$, system goes into a very complicated phase where the Lyapunov exponents become mainly positive.

4.1.3 Our approach on Lyapunov exponent

In the previous section, we explained the general definition of the Lyapunov exponent. In this section, we show our approach of extracting the largest Lyapunov exponent for the data studied in Paper I. To do that, we need the delay and the dimension to construct the phase portrait.

To construct the phase portrait, we choose the QCL bias $U(t)$ as the state variable out of our 223 variable system (from the data studied in Paper I). Then, we introduce a three dimensional vector to define the phase space, $v(t) = [U(t), U(t - \tau), U(t-2\tau)]$ operate in time where τ is the delay time. Here, the main idea is to choose a proper τ to provide information on how much is the correlation between the state variables.

Following Ref. [83], we use mutual information to retrieve an optimal τ. First, we extract the minimum and maximum points of the time series of $U(t)$. Following the division of the distance between the minimum and maximum points into N bins, we could introduce the mutual information as

$$I = \sum_{i=0}^{N} \sum_{j=1}^{N} P_{i,j}(\tau) log \frac{P_{i,j}(\tau)}{P_i P_j} \tag{4.9}$$

where P_i and P_j are the probability of the data at bins i and j and $P_{i,j}$ is the joint probability of the data in bin i and in bin j. Here in Eq. 4.9, we show the amount of information is gathered in average time t and $t + \tau$. In case of large delay time

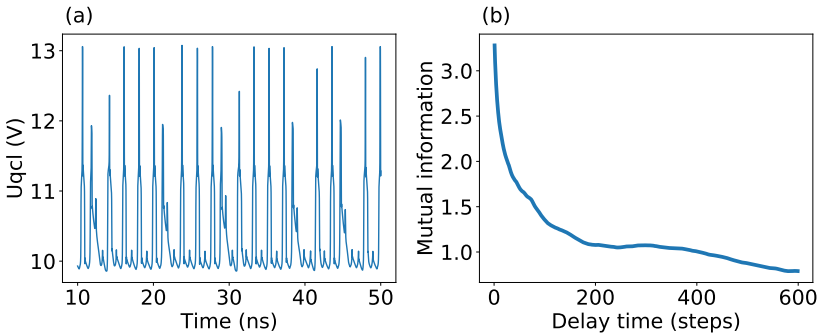

Figure 4.5: Time series in (a) and the mutual information in (b) are shown. The QCL voltage data is taken from Paper I for external voltage of $U_0 = 57$ (V).

of $\tau \to \infty$, for a chaotic system, the joint probability distribution will approach to $1/N$ and the mutual information disappears. Here, we choose smallest τ as the optimal delay and this provides smaller I for the data we have.

In Fig. 4.5(a), we show the time series of the QCL bias $U(t)$ studied in Paper I. The operation point is chosen where the oscillations are quite irregular. In Fig. 4.5(b) we show the mutual information based on Ref.[83] to extract the delay time. Here, a significant decrease in mutual information is observed around 200 delay time and following this point, higher delays does not seem to correlate. Thus, we obtain the proper delay time as of this point.

The dimension on the other hand provides recreation of the multidimensional systems [84]. Such as the Lorenz system, $d = 3$ is chosen to reveal the three dimensional structure. Regarding to the amount of coupled differential equations, more dimensions can be formulated. In paper I the device has the dimension of 223 which is the total number of the modules and the cavity modes.

With the extraction of the delay time and knowing the dimension of the system, it is now possible to construct a phase space for a vector of $U(t)$, $U(t+\tau)$ and $U(t+2\tau)$. To calculate the Lyapunov exponent we first start iterating the vector from t_0 to a point t_1. Here at t_1, both three components are approximately same within certain dynamics. Then, we compare the distance between the trajectories. Initially this distance is small. By iterating time, in case of chaos, the distance grows larger with $e^{\lambda t}$. This deviation provides the Lyapunov exponent and the system exhibit chaos if $\lambda > 0$. In paper I, we use the model introduced in Ref.[81] to

calculate the largest Lyapunov exponent.

4.1.4 Phase Portraits

In non-linear dynamical systems, phase portraits are common ways to visualise the trajectories of the time evolution of the systems [85, 86, 87, 88, 89]. The phase portraits are usually introduced in multidimensional systems which are defined by more than one state variables (e. g. angles and the angular velocities in the coupled pendulum). In this section, we study and compare the phase portraits of the Lorenz model and the QCL bias studied in Paper I.

The reason of choosing the Lorenz model and the THz QCL is that they are both autonomous chaotic systems. Which means that no time dependent external drive is applied. The external driving usually shows up in two ways. One way is to put the system out of it's equilibrium and this is usually the case in all physical systems. As the system in equilibrium goes into a stationary thermal state, they do not exhibit chaos. Thus, all chaotic systems need a driving to be pushed out of equilibrium. The second one is the existence of a time dependent (periodic) driving. Usually, if we have an oscillating non-linear system with a specific frequency (e. g. RC circuit or a single pendulum), adding an additional periodic driving with another frequency forces the system to be in two separate frequencies and resulting in complex phase portraits.

To construct phase portraits, at least a 2-D vector is required for a system defined by time dependent differential equations and 3-D vector for time independent system. For a time independent system, a point inside the limit cycle of a 2D phase will converge to the limit cycle (unless they escape to infinity) since the two points can not intersect with the stable point by different trajectories. They will either approach or diverge from the stable point. This is not the case of a time dependent system since the two points in the limit cycle can be at the same point in different times with different directions. Here, the Lorenz model is defined by time independent differential equations. Thus, the phase portrait is constructed three dimensional.

Following Ref. [90], we now introduce the set of equations to define the temperature gradient inside the earth atmosphere due to the incoming radiation from the sun. Regarding the up and down motion of the warm and the cold weather plates, interaction between them result in friction (e. g. Benard cells [91]). If the temperature difference between the cold and the warm plates become large enough, they

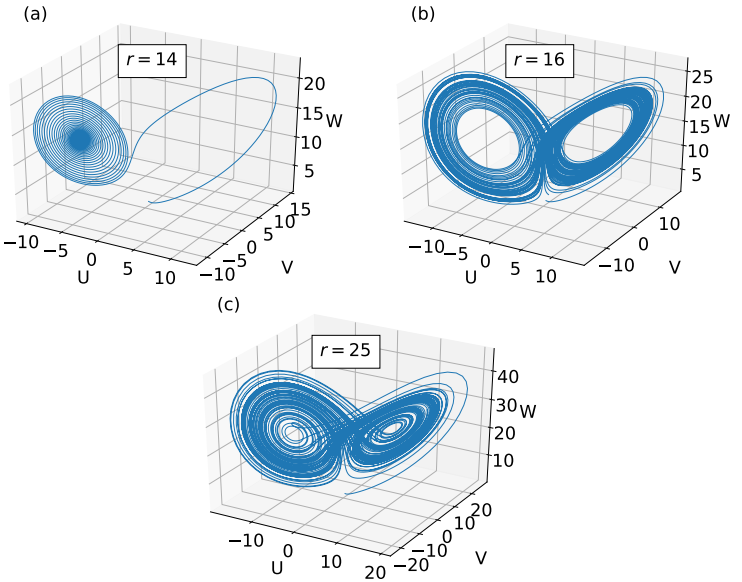

Figure 4.6: 3D phase portrait of the Lorenz map following the control parameters of $r = 14, 16, 25$ in (a), (b) and (c) respectively.

overcome the friction and start moving. This will cause vortexes. Following the increase in temperature difference up to a critical value, the system exhibits a period doubling scenario. To understand this, a set of non-linear equations are defined to show the flow between these two plates. This is also known as the atmospheric convection [92, 93]. To model this, Lorenz introduced three set of equations

$$\begin{aligned} \frac{dU}{dt} &= \alpha(V - U) \\ \frac{dV}{dt} &= U(r - W) - V \\ \frac{dW}{dt} &= UV - \beta W \end{aligned} \tag{4.10}$$

Here, U is defined as the rate of convection and V and W denotes the change in the temperature in both horizontal and vertical directions. In addition, the three constants α, r and β are the Prandtl number, Rayleigh number and the dimension of the layers respectively.

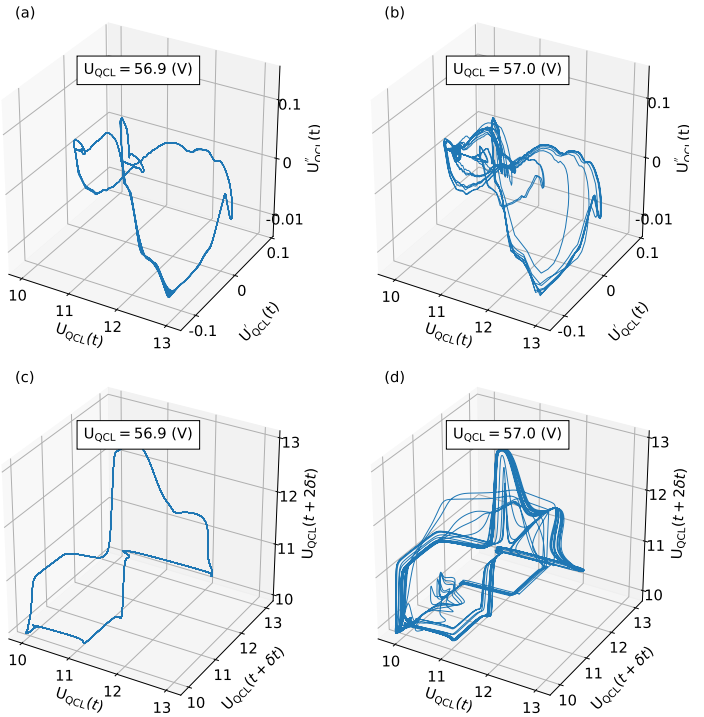

Figure 4.7: 3D phase portraits of the QCL voltage oscillations for the data studied in Paper I. External applied voltages are highlighted with the white boxes. In panels (a) and (b) we show the phase portrait with respect to first and second time derivatives of the U_{QCL} data. In panels (c) and (d) the phase portrait is constructed by adding the delay times τ and 2τ.

Solving these equations results in visualization of the three dimensional phase portraits with the control parameter r as seen in Fig. 4.6. Here, Prandtl number $\alpha = 10$ and dimension of the layer $\beta = 2.667$ is used as fixed parameters. One can easily see the transition of a system from regular to complex with only changing a single control parameter of r where the phase portrait become dense.

Fig. 4.7 shows the similarities of such transition to complexity in the phase portraits for the QCL voltage data studied in Paper I. Here, a long transience of 100 ns is cut and the following 30 ns are shown (the respective time series are shown in Fig.6 in Paper I). In the upper panels (a) and (b) the second and the third variables are chosen as the first and the second time derivatives of the voltage respectively. In

the bottom panels (c) and (d), QCL voltage is shown with respect to the selected delay times of $\tau = 0.2$ ns where the time steps in the data are 1 ps. Thus, 3D visualisation is provided to show the evolution of the trajectories. The control parameter is the external voltage U_0 and from panel (a) to (c) is shown in increasing order. A noticeable extension of the trajectories in the phase portraits observed as a complex structure at $U_0 = 57.0$ V. Thus, the transitions of the distinguishable paths in (a) and (c) to a much complex scenarios in (b) and (d) are shown.

4.2 Examples of Complex Systems

In the real world, most systems are tend to act as dissipative since many conditions result in losing the dynamical properties such as friction, thermal effects and etc. However, in case of applying a time dependent driving force to the losses from the dissipation balance each other with the driving force. This creates conditions for the system to evolve by its own behaviour as mentioned previously in Sec.4.1.4. Thus, in the presence of a time dependent driving, some systems exhibit chaos [94, 95, 96, 76]. This is not the case in Paper I where the chaotic behaviour in QCL is observed without a periodic driving. In this section, we show two such autonomous time dependent systems exhibit chaos; coupled pendulum and three body model.

One general example of such a chaotic system without periodic driving is the coupled pendulum [98, 99, 100, 101, 102] with the common stretching and folding behaviour of its phase space [103, 71, 104]. Here in Fig. 4.8 we show the illustration of the double pendulum scenario in (a) and the time series of the angles θ_1 and θ_2 in (b). The phase spaces are illustrated by choosing the angular velocities $\dot{\theta}_1/\dot{\theta}_2$ as a function of θ_1/θ_2 in (c) and (d). In panel (b), both time series exhibits complex oscillations. This is shown more clearly in panel (c) and (d) where the extend of the trajectories in each case spread around the phase portraits.

Another example of time dependent autonomous system is the three body model [106]. An example of the trajectories of three coupled stars as a function of time are shown in Fig. 4.9. The model is based on adding an additional celestial object (third star) to the coupled system of Alpha Centauri A and B. Solving the equation of motion provide the trajectories of these stars. As the time evolves, a very complex portrait reveals. Here, the code and the model is taken from the independent work done by Ref. [105].

In this Chapter, we briefly aimed to provide necessary information for the back-

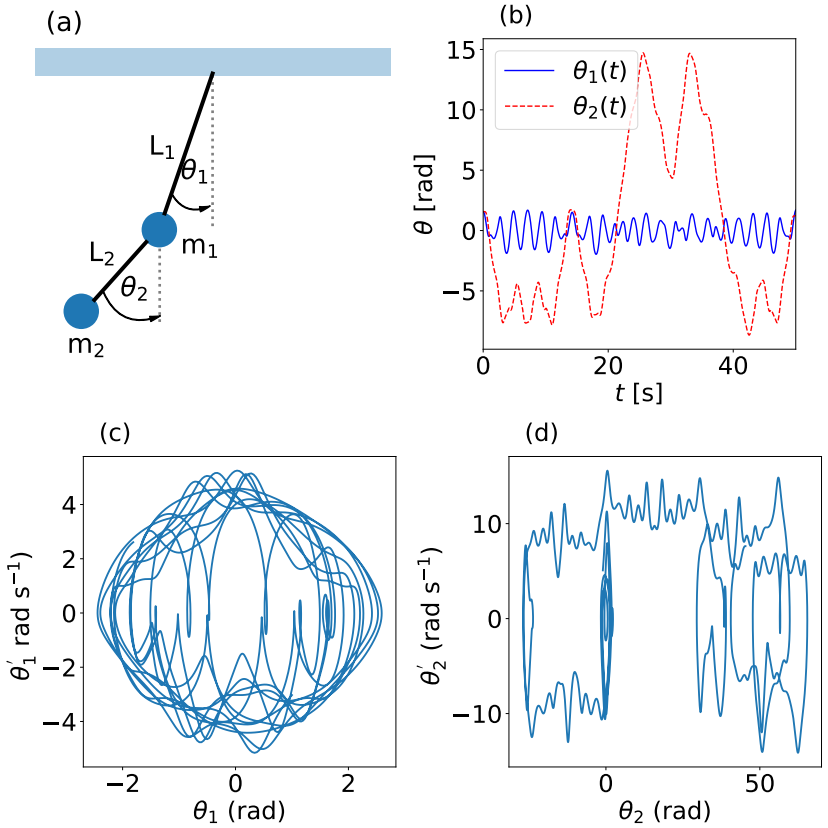

Figure 4.8: Illustration of the coupled pendulum including the constant parameters of masses $m_1 = 3$ and $m_2 = 1$ kg and lengths $L_1 = 1$ and $L_2 = 2$ m in (a) is shown. Time evolution of the angles θ_1/θ_2 in the range between 0 and $\pi/2$ are shown in (b) and the constructed phase portraits for the respective angles with the angular velocities are shown in (c) and (d). The background calculations for the code including the constants are adapted from Ref. [97].

ground ideas of implying the chaos models to the THz QCL device. As discussed above, in Paper I we show such scenarios of complex phase portraits, bifurcations as well as positive Lyapunov exponents. Our calculations show that an autonomous QCL exhibiting chaos without periodic drive is possible. Another study shows chaos in QCLs in Ref. [95] but with applying a periodic drive. Thus, the device studied in Paper I is the only autonomous QCL up to far.

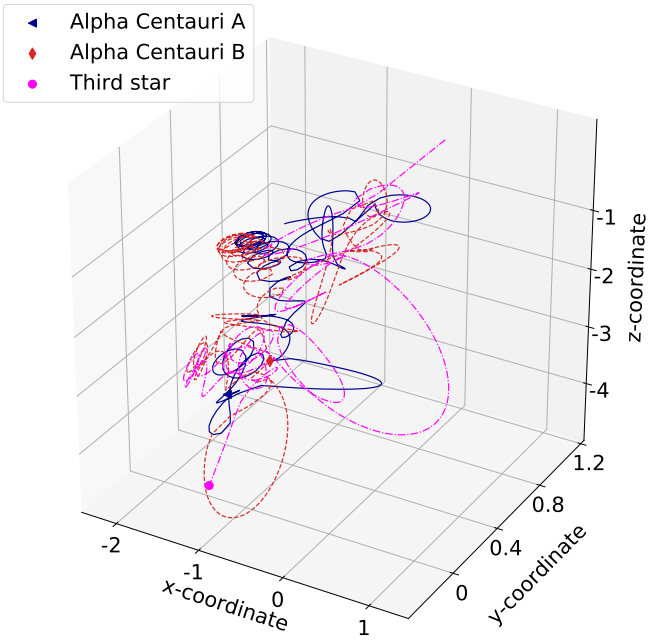

Figure 4.9: Illustration of the trajectories of a three body model. Three stars are chosen to model the time evolution of the coupled system. The python code is taken from Ref. [105]

Chapter 5

Low Frequency THz Quantum Cascade Lasers

The NEGF package has been used for large variety of simulations such as a systematic study of different structures [67] demonstrating its quantitative results. In paper II, we used it to understand and improve the temperature performance of the two-well QCLs operating around 4 THz. In this chapter, we use our NEGF package to provide typical results of the temperature performances of low frequency QCLs operating around 2THz. We first introduce the heterostructures to show the injection and extraction schemes. This is followed by the simulation of non-lasing current densities for two different conduction band offsets (CBO). Thus, the approximate barrier heights are extracted by comparing the maximum simulated and experimental current densities. This may reflect differences in the calibrations in different labs (see the corresponding discussion in Paper II). The quality of the designs with temperature is shown by the resolved current densities in order to identify the leakage current and temperature dependent mechanisms. Finally, we show the temperature dependent current densities and gain. Additionally, we also show our on going project of achieving the highest operation temperature at lower frequencies based on the LU2022 devices studied in Paper II.

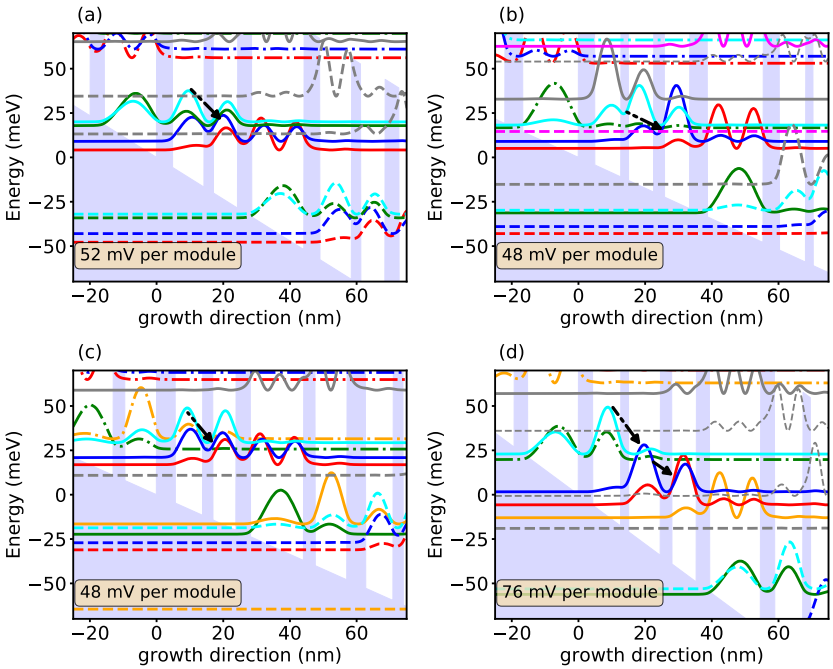

Figure 5.1: Wannier-Stark states at peak currents of four THz QCL design based on GaAs as wells and AlGaAs as barriers. The lasing transitions are shown by arrows and the applied biases at the current peak are highlighted by orange boxes on left bottom corners. The devices studied in (a), (b), (c) and (d) are ChassagneuxIEEE2012, KumarAPL2006, WilliamsElecLett2004 and KumarNature2010 respectively. Phonon temperatures are fixed in each panel to 150 K.

5.1 Applications of the NEGF Package

In this section, we study in detail four specific structures labelled by ChassagneuxIEEE2012 (the device operating at 2.3 THz in the article) [24], KumarAPL2006 [107], WilliamsElecLett2004 [108], and KumarNature2011 [26]. Each design is simulated using the layer sequences and sheet doping densities defined in the related articles. Note that, in the simulations the effected masses in the conduction band is taken as $m_{\text{eff}} = 0.067 + 0.083x$ and the root mean square of interface roughness is $\eta = 0.23$.

The heterostructures of the devices are shown in Fig. 5.1 with the Wannier-Stark states at resonance (at $J_{\max}$). Each device has the energy separation of around

Wafer	$J_{\max}^{\exp}$ (kAcm^{-2})	$J_{\max}^{\mathrm{sim}}$ (kAcm^{-2})	CBO (eV)
ChassagneuxIEEE2012	1.18	1.12	0.831x
		0.78	1.01x
KumarAPL2006		0.247	0.831x
	0.18	0.17	1.01x
WilliamsElecLett2004		0.82	0.831x
	0.64	0.58	1.01x
KumarNature2010		0.85	0.831x
	0.75	0.69	1.01x

Table 5.1: Table shows the experimental and simulated maximum currents. The simulated currents are shown for two different CBOs.

34-38 meV between the extraction and injection levels. This is close to the LO phonon energy $\hbar\omega_{\mathrm{LO}} = 36$ meV of GaAs. Thus, LO phonon extraction is the mechanism of quick depopulation of the lower states in each design. In panels (a), (b) and (c) the common resonant tunneling scheme is used to populate the upper levels.

In panel (d), scattering-assisted injection is used to achieve inversion. The device in (d) has a quite engaging design since the lasing transition is divided into two separate branches as shown by the arrows. The first transition is achieved with populating the upper state by resonant tunnelling via the injection barrier. The lasing transition occurs here with the frequency of around 3.6 THz. The carriers in the lower state travel to the closest energy level in the next well. This generates a second inversion followed by a lasing transition in a smaller lasing frequency of around 1.9 THz. This is due to the design which is aimed to maximise the current flow in higher voltages than the alignment of the injector and upper laser levels [26].

Following Table. 5.1, simulated currents are compared with the experimental values in the purpose of deciding the approximate barrier heights. To match the currents, we use two band offsets as barrier heights $0.831x$ eV and $1.01x$ eV following Refs. [67, 109]. The decision for each device is done by comparing the maximum current densities $J_{\max}$ and characteristics. Here, in ChassagneuxIEEE2012, the difference between the currents is 0.06 kAcm^{-2} for $0.831x$ eV and 0.4 kAcm^{-2} for $1.01x$. This comparison allows us to choose the smaller

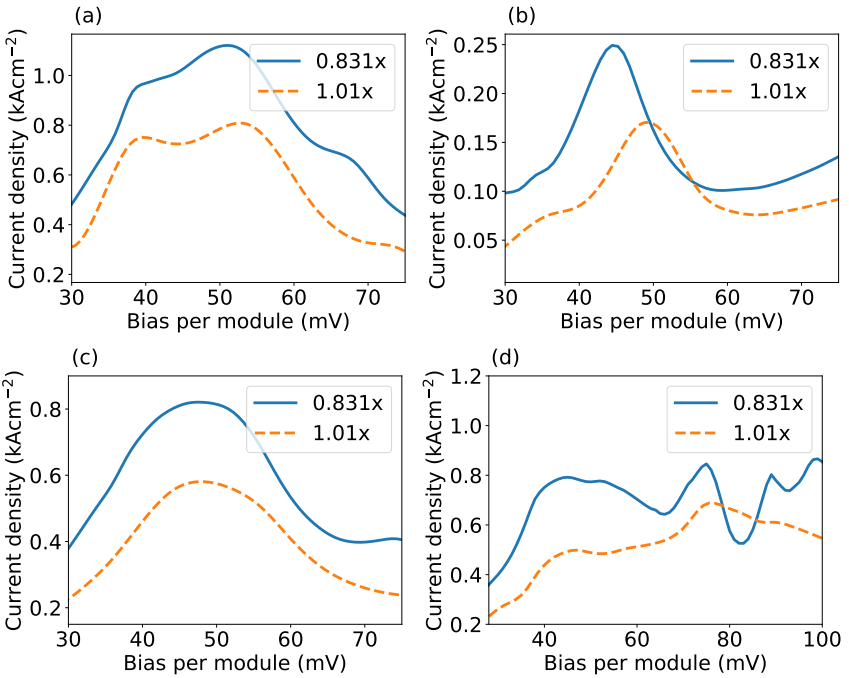

Figure 5.2: Current and bias relation without lasing is shown for four structures discussed in Fig. 5.1. Full lines are calculated with $0.831x$ eV and dashed lines are with $1.01x$ eV conduction band offsets. The devices studied here are ChassagneuxIEEE2012, KumarAPL2006, WilliamsElecLett2004 and KumarNature2010 for (a), (b), (c) and (d) respectively. Phonon temperatures are fixed in each panel at 150 K.

CBO of $0.831x$ eV for the further simulations. Similar comparisons are done for the rest of the devices and for both KumarAPL2006, WilliamsElecLett2004 and KumarNature2010, CBO of $1.01x$ eV is used in the following simulations. This follows the observation in Paper II that our simulations for MIT sample require an increased CBO value.

Fig. 5.2 shows the simulated non-lasing current densities for each device shown in Fig. 5.1 with the same order of labelling. ChassagneuxIEEE2012 exhibits the highest current with $J_{\max} = 1.12\,\mathrm{kAcm}^{-2}$ whereas the KumarAPL2006 has the lowest with $J_{\max} = 0.170\,\mathrm{kAcm}^{-2}$. It is expected that due to the decrease in tunneling amplitudes while the barrier height increases, current density drops. In

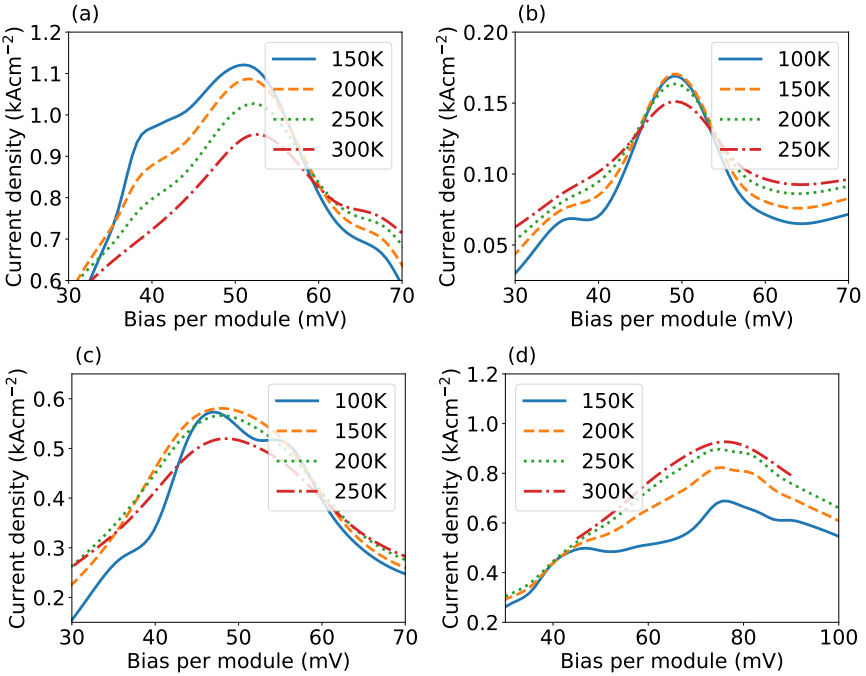

Figure 5.3: Current densities and bias relation without lasing is shown for four structures discussed in Fig. 5.1. Phonon temperatures are listed in the legends. The devices shown here from panel a to d are as follows: ChassagneuxIEEE2012, KumarAPL2006, WilliamsElecLett2004 and KumarNature2010

Fig. 5.2 we show such scenarios where in each device, average current densities drop by 30% as the barrier heights increase. The reason of using various numerical approximations on band offsets may be related to different calibrations and measurements of the barrier heights by separate groups.

5.1.1 Temperature Dependence of Current

Currently, one of the main challenge is to maximize the operation temperature in THz QCLs [110]. After a long period of time following the achievement of the operation at 199 K [111], the highest operation temperature of 250 K in pulsed mode was achieved [109]. Obtaining the population inversion in higher temperatures is quite difficult as several mechanism have impacts on the inversion. For instance, when the energy spacing between the upper and lower laser levels is less

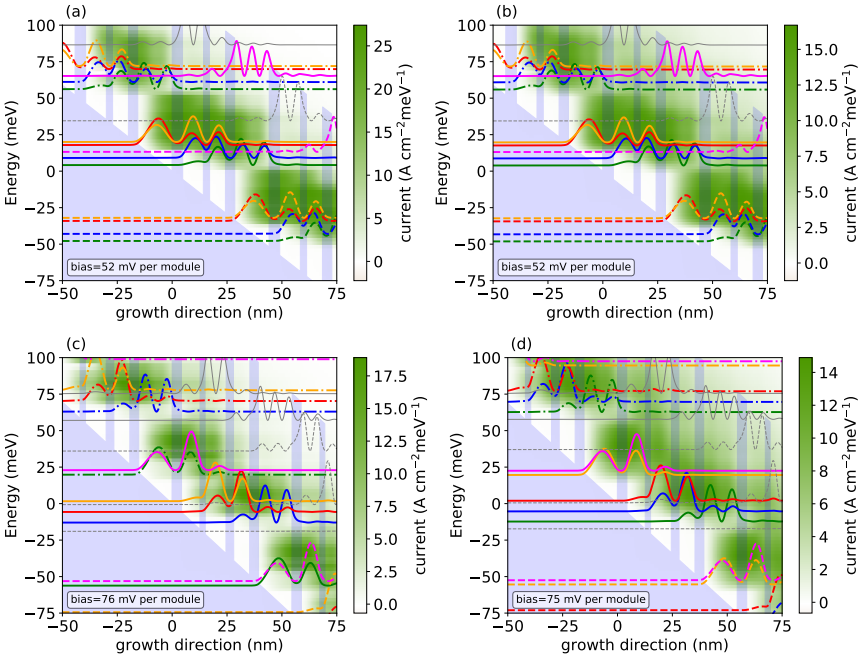

Figure 5.4: Spatially and energetically resolved current densities for devices ChassagneuxIEEE2012 in (a) and (b) and KumarNature2010 in (c) and (d). Horizontal panels are the same devices with different temperatures. Following 150 K in (a) and (c) and 300K (b) and (d) are used.

than the LO phonon energy of 36 meV, LO phonon scattering allows thermally excited electrons to relax from the upper to the lower laser level. This mechanism depopulates the upper laser level and diminishes the inversion. Also, the thermal backfilling mechanism studied in Paper II is shown as one of the detrimental effects on the inversion. This is the case when electrons in the extractor level absorbs an optical phonon and travels back to the lower laser level followed by a decrease in the inversion. In addition, the leakage of the hot carriers from laser states to the continuum results in barrier leakage. Overall, the achievement of sufficient inversion fails and gain does not surpass losses. This prevents desired lasing operation at higher temperatures [8].

Fig. 5.3 shows the simulated non-lasing current densities as a function of simulated phonon temperatures. In KumarAPL2006 and WilliamsElecLett2004 shown in (b) and (c), there are no substantial changes in the current densities with tempera-

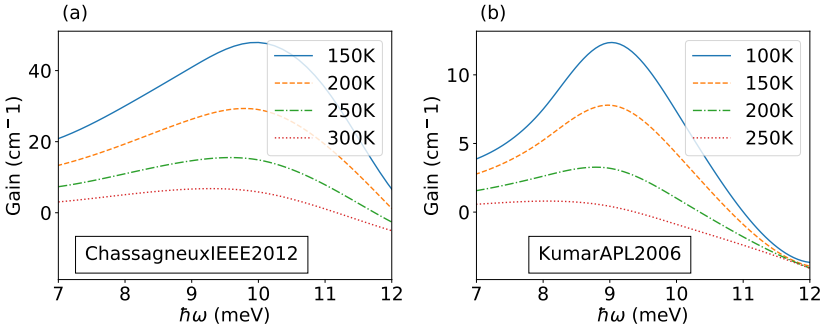

Figure 5.5: Linear response gain calculated by our NEGF model for $eF_{ac}d = 0.1$ meV as a function of phonon temperature. The simulated devices are highlighted in the boxes at top right corners.

ture followed by a slight decrease at 250 K. In KumarNature2010 shown in (d), the current density increases with the phonon temperature due to the large spatial extend of the leakage current. This results in dissipation of higher powers, reducing efficiency and heating of the lattice. In contrast, with increasing phonon temperature the current density decreases in ChassagneuxIEEE2012 shown in panel (a). This trend may arise where our model fails to capture the escaping currents through the continuum at the edges of the barriers. Regarding to the characteristics, in each panel of Fig. 5.3 the curvatures in the current densities at the low field range vanish with the phonon temperature.

In Fig. 5.4 we show the energetically and spatially resolved currents for the two devices exhibiting the strongest temperature dependence. In the horizontal panels (a) and (b), resolved currents for ChassagneuxIEEE2012 device is shown for 150 K and 300 K respectively. Similarly in the bottom panels, resolved currents for KumarNature2010 device is presented for 150 K in (c) and 300 K in (d). In both devices, as the phonon temperatures raise, the spatial extends of the current densities significantly increase in (b) and (d). This is due to the thermally activated scattering of the carriers to the higher states and their escape from the barriers to the continuum. Additionally, we observe that the spatial extend of the currents between the upper level and the extraction level caused by LO phonon emission as well as the LO phonon emission from the lower laser level to the higher states. Similar behaviour is observed in WilliamsElecLett2004 and KumarAPL2006 with slight variations.

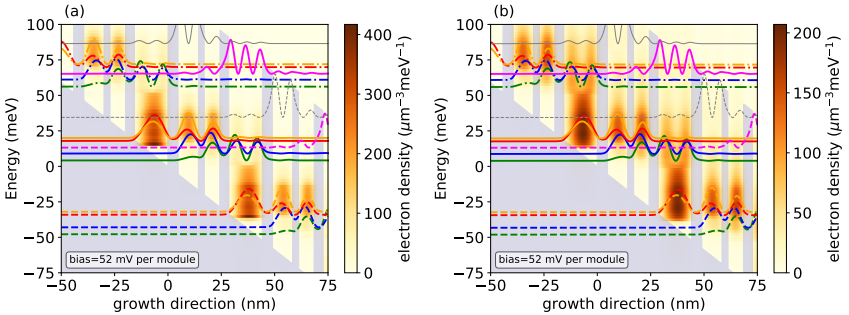

Figure 5.6: Spatially and energetically resolved densities for ChassagneuxIEEE2012 are shown. Phonon temperatures are 150 K in (a) and 300 K in (b). The module biases at resonance are highlighted by the boxes in the lower left corners.

5.1.2 Temperature Dependence of Gain

The objective of designing QCLs is to achieve light i. e. substantial gain is required. Favorably, more population in the upper and less in the lower laser levels are desired to achieve higher inversion. As the thermally scattering mechanism are of significance, the gain is detrimentally affected by the temperature due to the decrease in inversion. In this section, we show the effects of phonon temperatures on resolved electron densities and gain. Also, we show a systematic approach to understand the difference between experimental heatsink and simulated phonon temperatures for the four THz QCLs studied previously.

In Fig. 5.5, simulated linear response gain as a function of frequency is shown for ChassagneuxIEEE2012 and KumarAPL2006. The phonon temperatures are varied and due to the scattering and backfilling mechanisms, the gain substantially drops as the inversion diminishes. In each panel, the overall drop in gain is approximately 40% for 50 K steps. Similar trends are observed for the other devices with small variations.

Fig. 5.6 shows the spatially and energetically resolved electron densities for the ChassagneuxIEEE2012 device for two different phonon temperatures. It is quite clear that the injector and the upper laser level share the most of the carrier densities in both panels. This is due to the resonant tunneling injection scheme where almost half of the carriers occupying the upper laser levels. Here, one could easily identify that the lower laser levels are almost empty at 150 K in panel (a). This

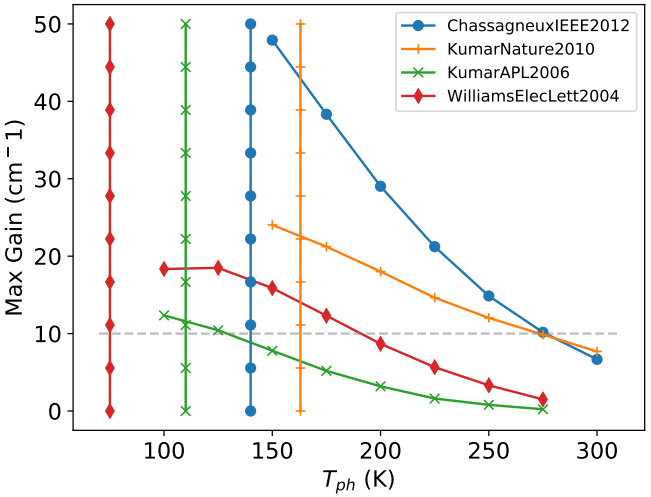

Figure 5.7: Maximum gain as a function of phonon temperatures are shown for the devices shown in Fig. 2.1. Vertical lines are the maximum heatsink temperatures of the devices in pulse mode. Same markers represents the simulation and experimental temperatures of the same devices. Horizontal dashed line represents the waveguide and mirror losses $g = 10$ cm^{-1}.

shows that the optimal operation point is chosen. Increasing phonon temperature results in significant thermal backfillings to the lower laser level from the upper laser and the extractor level as seen in (b) (see Paper II for further analysis on the thermal backfilling mechanism). This detrimentally decreases the inversion and the gain drops approximately 60% following the Fig. 5.7. Similar scenarios are also observed in other devices with slight variations.

To provide a general picture, the simulated maximum gain as a function of simulated phonon temperatures are compared with the experimental maximum heatsink temperatures in Fig. 5.7. The vertical lines are the experimental maximal heatsink temperatures of the devices which are naturally lower than the simulated phonon temperatures. To guide the eye, we use same markers to compare experimental and simulated data for each device (e. g. diamond marker is used for WilliamsElecLett2004). The waveguide and mirror losses are assumed to be 10 cm^{-1} for the metal-metal waveguides following the approximations in Ref. [67] for lasing frequencies between 1.7 and 2.5 THz. This is visualised by the horizontal dashed line. Here, KumarNature2010 and ChassagneuxIEEE2012 have the highest op-

Wafer	$J_{\max}^{\exp}$ (kAcm^{-2})	$T_{\max}^{\mathrm{sim}}$ (K)	$T_{\max}^{\exp}$ (K)	f_{sim} (THz)	$f_{\exp}$ (THz)
(A)	1.18	275	140	2.41	2.3
(B)	0.75	275	163	2.17	2.1
(C)	0.64	175	72	1.85	1.8
(D)	0.18	125	110	1.93	1.9

Table 5.2: Table shows the maximum experimental heatsink and simulated phonon temperatures, peak currents and the experimental and simulated (at maximum gain) lasing frequencies. The devices are labelled following the same ordering with the peak currents as: ChassagneuxIEEE2012 (A), KumarNature2010 (B), WilliamsElecLett2004 (C) and KumarAPL2006 (D)

eration temperatures in experiments and this is consistent with our simulations with the phonon temperatures slightly larger than the heatsink temperatures.

In Table. 5.2 we show the summary of the maximum heatsink and the phonon temperatures as well as the experimental and simulated lasing frequencies for each device. The table shows that our choice of operation points are consistent as the simulated lasing frequencies match with the experimental ones. In KumarNature2010 and ChassagneuxIEEE2012 which exhibits the highest currents, the simulated gain surpass losses up to 275 K. This represents to a temperature difference of 112 K in KumarNature2010 and 135 K in ChassagneuxIEEE2012 with the maximum heatsink temperatures. These considerable differences may be explained by the choice of the waveguide and mirror losses. A similar case is also seen in WilliamsElecLett2004 with a phonon and heatsink temperature difference of around 103K. On the other hand in KumarAPL2006, the simulated phonon temperature fits well with a difference of 15K with the experimental heatsink temperature which is the device with lowest current. The order of the difference between the heatsink and phonon temperatures are studied in detail in Paper II and in Refs. [112, 113].

To summarize, a difference of about 100 K seems to suits well with most of the devices similar to Paper II for 4 THz QCLs. Here, we observed that the difference in simulated phonon and the experimental heatsink temperatures decreases proportionally with the maximum currents. It is quite ambitious to state a systematical approach as we could not have a viable model embedded to the temperature

differences for all the devices. More information about the actual losses due to the waveguide and mirrors are needed to fully quantify the differences.

5.2 High performing THz QCLs at low frequencies

Currently, the highest operation temperatures of THz QCLs are based on two-well designs studied in Paper II. Inspired by the design in Paper II exhibiting the highest operation temperature around 4 THz, here we provide new two-well designs based on the LU2022 device. The aim is to achieve highest operation temperature around 2 THz. To simplify, we label the structures with LU2022A and LU2022B where we increase the width of the lasing well and the extraction barrier to reduce the energy differences between the lasing levels. Here, the quantitative results are gathered by using our NEGF package.

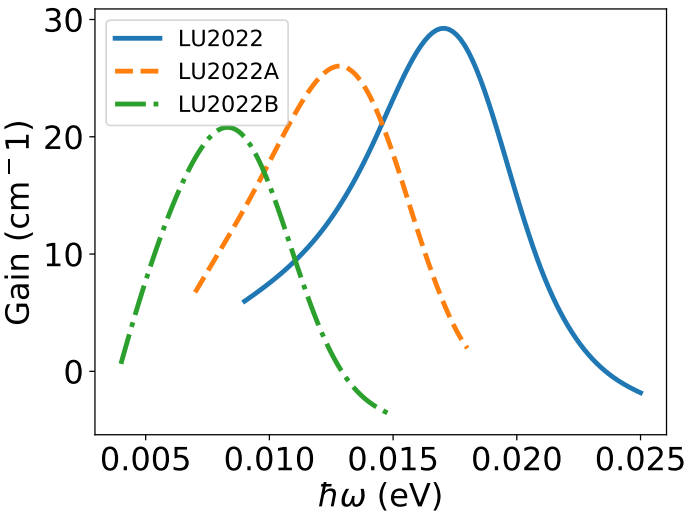

Figure 5.8: Gain as a function of frequency for the devices LU2022, LU2022A and LU2022B at phonon temperature of 300K.

The operation in the lower frequencies are achieved by the combination of increasing the lasing well and the extraction barrier. In Fig. 5.8, we show the gain spectrum of each device at phonon temperatures at 300 K showing gain above 20 cm^{-1}, which is a conservative estimation for losses. Increasing the lasing well and the extraction barrier results in a decrease in maximum gain while the lasing frequencies shift to the lower branches. With using the same approximation in

Wafer	Seq. (nm)	J_{max}^{sim} (kAcm^{-2})	g_{max} cm^{-1}	f_{sim} (THz)
LU2022	**3.1**/7.1/**2.1**/14.2	2.52	29.3	4.1
LU2022A	**3.1**/7.3/**2.2**/14.2	2.55	26	3.1
LU2022B	**3.1**/7.6/**2.4**/14.2	2.54	20.6	1.93

Table 5.3: Layer sequences of the suggested two new devices LU2022A and LU2022B. Maximum current densities , maximum gain and the lasing frequencies at a phonon temperature of 300 K are shown.

Paper II, we use a difference of 90K between the simulated phonon and the experimental heatsink temperatures. This indicates lasing operation well above 200 K where thermoelectric cooling is possible [114].

Here in Tab. 5.3, we show the layer sequences, simulated maximum current densities, maximum gain and the lasing frequencies for the related devices. Increasing the lasing well and the extraction barrier results in a systematical increase in the maximum current density while the lasing frequencies decrease. Even if the gain drops substantially, at 1.93 THz, it matches the losses and the lasing operation is achieved. Here, with the approximation of 90 K difference between the phonon and heatsink temperatures yields the experimental operation at 210 K around 1.93 THz is possible. This is the highest operation temperature in the related frequency range and can allow technological applications with thermoelectrical cooling [114, 115].

Chapter 6

Summary and Outlook

In this thesis, we provided new insights into contemporary issues of THz QCLs such as higher temperature operation, analysing the electric field distribution in the presence of NDC, and chaotic output signals.

First, we provided microscopic simulations with our NEGF package to extract quantitative results for current and gain for THz QCLs. We could identify structures operating up to 265 K around 4 THz as published in Paper II. This would constitute a new record temperature operation and enable devices which require very little cooling. Moreover in Chap. 5, we expanded this operation principle to lower frequencies down to 2 THz. Our findings suggest that the thermoelectrical cooling is possible for devices in the entire range of 2 to 4 THz.

The formation of the electric field domains is studied extensively in this thesis with two different aspects. First, we studied how the interaction of the electric field domains with the light field can broaden the effective gain spectrum of the device in accordance with recent experimental findings as discussed in Paper III and Chap. 3. This allows to produce samples with wider frequency coverage of the spectrum and is relevant for generating frequency combs.

Furthermore, we showed that the interaction of electric field domains with the light field can result in chaotic behaviour. This is shown in Paper I and Chap. 4 where we observed the first autonomous QCL exhibiting chaos. Next to their fundamental interest such chaotic systems have been suggested to be applicable for secure communication systems.

The limitations of our model is the lacking description of the leakage to the continuum. This effects both the THz operation and the high field domains. Modelling this leakage could provide a more realistic model with consistent results for some devices. Also, expanding chaos to mid IR QCLs may increase the technological applicability. Additionally, we still wonder about the basic phenomenon limiting THz operation. It would be very interesting to learn whether operation below 1 THz is possible.

Appendix A

A.1 Rate equations and gain medium

The gain medium inside a two level system is usually treated by the rate equations and the Fermi Golden rule [13, 16]. These models are commonly used to solve quantum transport and gain inside such systems. The occupations of the states, transition rates, scattering life times as well the applied ac fields are the relevant variables. Here, we define the probe frequency as ω, dc voltage $F_{dc}d$ and the ac field F_{ac} respectively.

An illustration of the two level system is shown in Fig. A.1. Here the model includes the injected current J_i, particle populations n_1 and n_2, the scattering life times τ_1, τ_2 of levels 1 and 2 and the scattering life time from level 2 to level 1 $\tau_{2,1}$. The rate equations applied in Refs. [16, 30] are

$$\frac{dn_1}{dt} = \frac{n_2}{\tau_{2,1}} + \gamma_{1\to2}(\omega)F_{ac}^2\Delta n - \frac{n_1 - n_1^{therm}}{\tau_1} \tag{A.1}$$

and

$$\frac{dn_2}{dt} = \frac{J_i}{e} - \gamma_{1\to2}(\omega)F_{ac}^2\Delta n - \frac{n_2}{\tau_2} \tag{A.2}$$

Here in Eq. A.1 and Eq. A.2, the population inversion is denoted by $\Delta n = n_2 - n_1$ and the third term of Eq. A.1 represents the thermal equilibrium of the population without the injection current. In addition, we introduced the transition rate γ between the states by Fermi Golden rule. Assuming the gain spectrum is Lorentzian, the transition rate can be written as

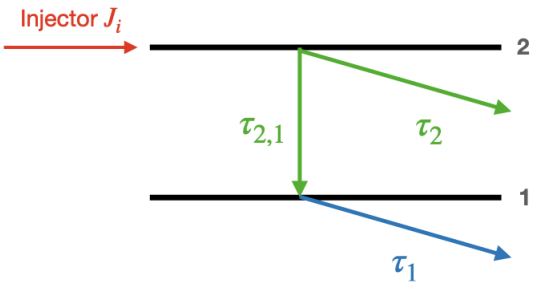

Figure A.1: An illustration of the two level gain medium inspired by [16]. The model includes in injection current J_i and scattering and transition life times τ.

$$\gamma_{1,2}(\omega) = \frac{\pi}{2\hbar}|ez_{1,2}|^2 \frac{1}{2\pi} \frac{\Gamma}{(\Delta E - E)^2 + \Gamma^2/4} \tag{A.3}$$

where z is the dipole matrix element between the states and separated from the ac field intensity F_{ac}^2.

Introducing the steady state conditions $dn/dt = 0$ to the rate equations and assuming $(\tau_{2,1} - \tau_1)/\tau_2 \approx 0$ as well as combining with Eq. A.1 and Eq. A.2 provide the population inversion as

$$\Delta n = -n_1^{therm} + \tau_2 \frac{J_i}{e} - (\tau_1 + \tau_2)\gamma_{1,2}(\omega)F_{ac}^2 \Delta n \tag{A.4}$$

The first two terms are the unsaturated populations while the last term is the saturation where the ac field intensity is relevant. The gain recovery time from the saturation can be estimated by $\tau_{\text{eff}} \approx \tau_1 + \tau_2$.

A.1.1 Our approach to gain and current

Our model is based on fitting the Lorentzian profile to linear and non-linear response gain obtained by homogeneous NEGF package. Starting with the definition of the linear response gain in Refs. [30], and the combination with the γ in Eq. A.3

$$G_0(\omega) = \frac{2\omega\Delta n}{c\sqrt{\epsilon_r\epsilon_0^2}d}\gamma_{1\to 2}(\omega) \tag{A.5}$$

The saturation of the gain with ac field intensity and including the life times of the upper laser level τ can be defined as

$$G(\omega,\omega^{'}) = \frac{G_0(\omega)}{1+\tau\gamma(\omega^{'})F_{ac}^2} \tag{A.6}$$

Here in Eq. A.6 the separation of the pumping $\omega^{'}$ and the probe frequency ω allows to control the saturation in selected frequencies. The Lorentzian in the denominator is taken into account to treat the power broadening. Thus the relevant term in saturation can be written as

$$\tau_i\gamma_i(\omega_i)F_{ac}^2 = \left|\frac{\pi z_i}{d}\right|\frac{(eF_{ac}d)^2}{\gamma_i^{ul}+\gamma_i^{ls}}\frac{1}{2\pi}\frac{\Gamma}{(\Delta E-E_i)^2+\Gamma^2/4} \tag{A.7}$$

Here, the term $|\pi z_i/d|$ with the matrix element z and the module length d is a dimensionless constant. The width of the transitions in the upper laser level γ^{ul} and the lower laser level γ^{ls} is calculated by saturation of the gain.

Our treatment of the current $J(\omega)$ is based on the laser transitions and the total current becomes the sum of the stationary and lasing induced currents

$$J(F_{\rm dc},F_{\rm ac},\omega) = J_0 + e\sum_i(n_u-n_i)\kappa(\omega,\omega_i)\frac{I(\omega)}{\hbar\omega} \tag{A.8}$$

Here, κ is the cross-section of the absorption and emission processes and the photon flux is described by the intensity I in the last term. As the inversion and the cross-section is related with the gain $G \approx (n_u - n_i)\kappa$. the current inside the modules can be written as

$$J(F_{\rm dc},F_{\rm ac},\omega^{'}) = J_0 + edG(\omega^{'})\frac{c\sqrt{\epsilon_r\epsilon_0^2}F_{ac}^2}{2\omega^{'}} \tag{A.9}$$

As the devices studied here have a clear gain distribution in Lorentzian shape, we are confident that our approach is suitable to obtain quantitative results.

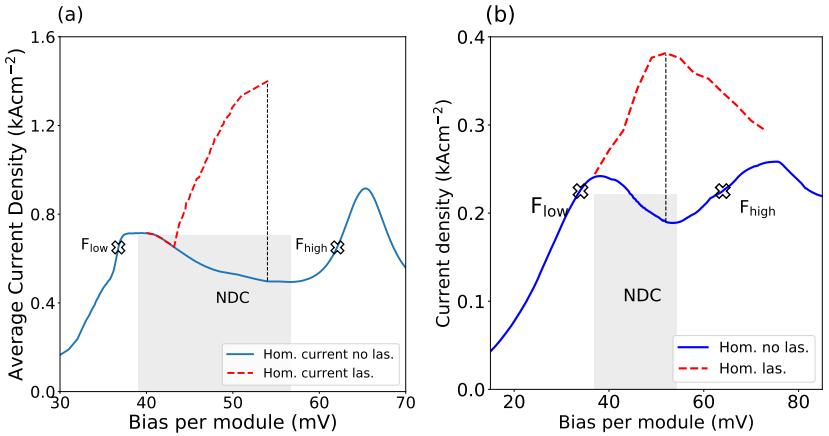

Figure A.2: Current bias relation for two THz devices V813 in (a) and EV2244 in (b). Full curves are the current without lasing as well as dashed curves represent current with lasing. Gray areas highlight the NDC regions as well as black vertical lines are the nominal operation points (NOP).

A.2 Extracting results from the NEGF package

Our domain model is based on fitting the homogeneous gain extracted from our NEGF package. Here, we show the current bias relation and the gain saturation with applied ac field which is proportional to the photon number in the cavity modes. The two devices shown here are labelled as V812 and EV2244.

Fig. A.2 shows the current bias relations of devices V812 and EV2244 with and without lasing. The simulations are done by fixed phonon temperatures at 77 K for V812 and 150 K for EV2244. Both devices exhibit two current peaks as discussed in Sec. 1.3 and the NDC region appears in between. V812 has relatively higher currents of up to 0.9 kAcm^2 than EV2244 of 0.25 kAcm^2. This shows that the threshold current is also lower in EV2244. The decrease in current after the resonance is avoided by applying an AC field strength F_{ac} as the additional photo-assisted current increases the total current. In each device, the nominal operation points (NOP) are located inside the NDC region and a stable operation can be achieved via applied ac field (red dashed curves). In panel (a) following the current with lasing, the lasing switches on around 42 mV inside the NDC. This is not the case in EV2244 where the lasing starts around the first current peak at 37 mV.

Using two separate ac fields strength of $eF_{\mathrm{ac}}d = 0.1$ and $eF_{\mathrm{ac}}d = 10$ meV,

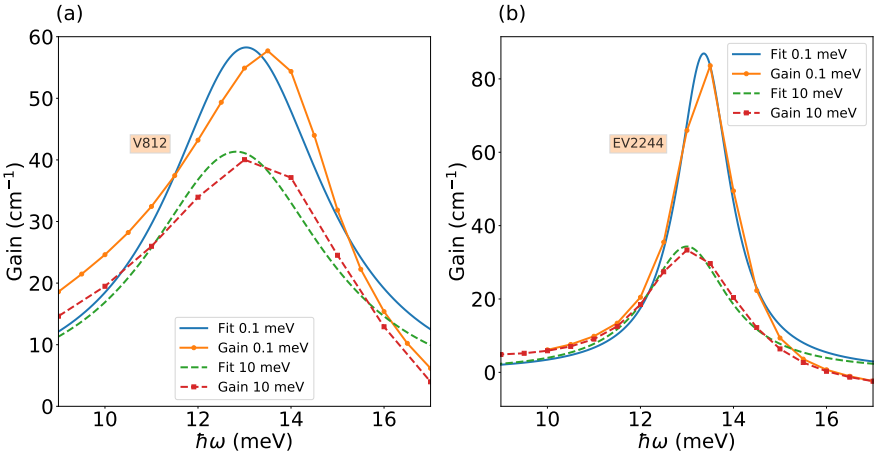

Figure A.3: Linear and non-linear response gain for two THz devices V812 in (a) and EV2244 in (b). In each panel full lines represent the linear response gain with $eF_{ac}d = 0.1$ meV and dashed ones represent non-linear response gain with $eF_{ac}d = 10$ meV. The data extracted from NEGF package is shown with square and round markers while full lines represents the fit. The phonon temperatures are 77 K in (a) and 150 K in (b).

we simulate the linear and non-linear response gain respectively for each device shown in Fig.A.3 at the NOP. Both devices have sufficiently large gain where the waveguide and mirror losses are accepted as 20 cm^{-1} following the approximations in Ref. [67]. Here, we use the Lorentzian distribution to fit the gain data to extract the width, amplitude and central frequency of the distribution. The results are used to calculate saturated gain and current in our inhomogeneous domain model.

Bibliography

[1] J. Faist, F. Capasso, D. L. Sivco, C. Sirtori, A. L. Hutchinson, and A. Y. Cho, *Quantum cascade laser*, Science **264**, 553 (1994)

[2] M. Beck, D. Hofstetter, T. Aellen, J. Faist, U. Oesterle, M. Ilegems, E. Gini, and H. Melchior, *Continuous wave operation of a mid-infrared semiconductor laser at room temperature*, Science **295**, 301 (2002)

[3] A. Szerling, K. Kosiel, M. Szymanski, Z. Wasilewski, K. Golaszewska, A. Laszcz, M. Pluska, A. Trajnerowicz, M. Sakowicz, M. Walczakowski, N. Palka, R. Jakiela, and A. Piotrowska, *Processing of AlGaAs/GaAs quantum-cascade structures for terahertz laser*, Journal of Nanophotonics **9**, 093079 (2015)

[4] B. McManus, M. Zahniser, D. Nelson, J. Shorter, S. Herndon, E. Wood, and R. Wehr, *Application of quantum cascade lasers to high-precision atmospheric trace gas measurements*, Optical Engineering - OPT ENG **49**, 111124 (2010)

[5] R. Lewicki, A. A. Kosterev, D. M. Thomazy, T. H. Risby, S. Solga, T. B. Schwartz, and F. K. Tittel, *Real time ammonia detection in exhaled human breath using a distributed feedback quantum cascade laser based sensor,* Proc. of SPIE Vol. 7945 , in *Quantum Sensing and Nanophotonic Devices VIII*, edited by M. Razeghi, R. Sudharsanan, and G. J. Brown, p. 79450K (SPIE, 2011)

[6] A. A. Lyakh, R. Maulini, A. G. Tsekoun, and C. K. N. Patel, *Progress in high-performance quantum cascade lasers*, Optical Engineering **49**, 111105 (2010)

[7] R. Köhler, A. Tredicucci, F. Beltram, H. E. Beere, E. H. Linfield, A. G. Davies, D. A. Ritchie, R. C. Iotti, and F. Rossi, *Terahertz semiconductor-heterostructure laser*, Nature **417**, 156 (2002)

[8] B. Wen and D. Ban, *High-temperature terahertz quantum cascade lasers*, Progress in Quantum Electronics **80**, 100363 (2021)

[9] K. Kosiel, J. Kubacka-Traczyk, P. Karbownik, A. Szerling, J. Muszalski, M. Bugajski, P. Romanowski, J. Gaca, and M. Wójcik, *Molecular-beam epitaxy growth and characterization of mid-infrared quantum cascade laser structures*, Microelectronics Journal **40**, 565 (2009), workshop of Recent Advances on Low Dimensional Structures and Devices (WRA-LDSD)

[10] G. Grynberg, A. Aspect, and C. Fabre, *Introduction to Quantum Optics* (Cambridge University Press, Cambridge, 2010)

[11] O. Svelto, *Pumping processes*, in *Principles of Lasers*, pp. 205–253 (Springer US, Boston, MA, 2010)

[12] D. J. Griffiths and D. F. Schroeter, *Introduction to Quantum Mechanics* (Cambridge University Press, 2018), 3rd edition

[13] J. J. Sakurai, *Modern Quantum Mechanics* (Addison Wesley, 1993), 1st edition

[14] J. H. Davies, *The Physics of Low-dimensional Semiconductors: An Introduction* (Cambridge university press, 1997)

[15] P. Y. Yu and M. Cardona, *Fundamentals of Semiconductors* (Springer, Berlin, 1999)

[16] J. Faist, *Quantum Cascade Lasers* (Oxford University Press, Oxford, 2013)

[17] W. T. Silfvast, *Laser Fundamentals* (Cambridge University Press, 2004), 2nd edition

[18] D. O. Winge, E. Dupont, and A. Wacker, *Ignition of quantum cascade lasers in a state of oscillating electric field domains*, Phys. Rev. A **98**, 023834 (2018)

[19] C. Sirtori, P. Kruck, S. Barbieri, P. Collot, J. Nagle, M. Beck, J. Faist, and U. Oesterle, *GaAs/AlGaAs quantum cascade lasers*, Appl. Phys. Lett. **73**, 3486 (1998)

[20] B. S. Williams, *Terahertz quantum-cascade lasers*, Nat. Photonics **1**, 517 (2007)

[21] C. Walther, M. Fischer, G. Scalari, R. Terazzi, N. Hoyler, and J. Faist, *Quantum cascade lasers operating from 1.2 to 1.6 THz*, Appl. Phys. Lett. **91**, 131122 (2007)

[22] M. Wienold, B. Röben, X. Lü, G. Rozas, L. Schrottke, K. Biermann, and H. T. Grahn, *Frequency dependence of the maximum operating temperature for quantum-cascade lasers up to 5.4 THz*, Applied Physics Letters **107**, 202101 (2015)

[23] B. S. Williams, S. Kumar, H. Callebaut, Q. Hu, and J. L. Reno, *Terahertz quantum-cascade laser operating up to 137 K*, Appl. Phys. Lett. **83**, 5142 (2003)

[24] Y. Chassagneux, Q. Wang, S. Khanna, E. Strupiechonski, J. Coudevylle, E. Linfield, A. Davies, F. Capasso, M. Belkin, and R. Colombelli, *Limiting factors to the temperature performance of THz quantum cascade lasers based on the resonant-phonon depopulation scheme*, Terahertz Science and Technology, IEEE Transactions on **2**, 83 (2012)

[25] S. Khanal, J. L. Reno, and S. Kumar, *2.1 THz quantum-cascade laser operating up to 144 K based on a scattering-assisted injection design*, Opt. Express **23**, 19689 (2015)

[26] S. Kumar, C. W. I. Chan, Q. Hu, and J. L. Reno, *A 1.8 THz quantum cascade laser operating significantly above the temperature*, Nat. Physics **7**, 166 (2011)

[27] J. B. Gunn, *Instabilities of current in III–V semiconductors*, IBM J. Res. Dev. **8**, 141 (1964)

[28] A. Wacker, *Semiconductor superlattices: a model system for nonlinear transport*, Phys. Rep. **357**, 1 (2002)

[29] B. Jovic, *Chaotic signals and their use in secure communications*, in *Synchronization Techniques for Chaotic Communication Systems*, pp. 31–47 (Springer, Berlin, Heidelberg, 2011)

[30] D. Winge, *Quantitative Modeling of Gain in Quantum Cascade Lasers under Operational Intensities*, Ph.D. thesis, Lund University (2016)

[31] A. Wacker, M. Lindskog, and D. O. Winge, *Nonequilibrium Green's function model for simulation of quantum cascade laser devices under operating conditions*, IEEE J. Sel. Top. Quant. **19**, 1200611 (2013)

[32] Franckie, Martin, *Modeling Quantum Cascade Lasers : The Challenge of Infra-Red Devices*, Ph.D. thesis, Lund University (2016)

[33] K. Lüdge and E. Schöll, *Quantum-dot lasers—desynchronized nonlinear dynamics of electrons and holes*, IEEE Journal of Quantum Electronics **45**, 1396 (2009)

[34] F. Capasso, J. Faist, and C. Sirtori, *Mesoscopic phenomena in semiconductor nanostructures by quantum design*, J. Math. Phys. **37**, 4775 (1996)

[35] F. Compagnone, A. Di Carlo, and P. Lugli, *Monte Carlo simulation of electron dynamics in superlattice quantum cascade lasers*, Appl. Phys. Lett. **80**, 920 (2002)

[36] D. Indjin, P. Harrison, R. W. Kelsall, and Z. Ikonic, *Self-consistent scattering theory of transport and output characteristics of quantum cascade lasers*, J. Appl. Phys. **91**, 9019 (2002)

[37] S. Tortora, F. Compagnone, A. Di Carlo, P. Lugli, M. T. Pellegrini, M. Troccoli, and G. Scamarcio, *Theoretical study and simulation of electron dynamics in quantum cascade lasers*, Physica B **272**, 219 (1999)

[38] R. C. Iotti and F. Rossi, *Carrier thermalization versus phonon-assisted relaxation in quantum cascade lasers: A monte carlo approach*, Appl. Phys. Lett. **78**, 2902 (2001)

[39] H. Callebaut and Q. Hu, *Importance of coherence for electron transport in terahertz quantum cascade lasers*, J. Appl. Phys. **98**, 104505 (2005)

[40] C. Ndebeka-Bandou, F. Carosella, and G. Bastard, *Quantum States and Scattering in Semiconductor Nanostructures*, Advanced textbooks in physics (World Scientific, 2017)

[41] C. Sirtori, F. Capasso, J. Faist, and S. Scandolo, *Nonparabolicity and a sum rule associated with bound-to-bound and bound-to-continuum intersubband transitions in quantum wells*, Phys. Rev. B **50**, 8663 (1994)

[42] S. R. White and L. J. Sham, *Electronic properties of flat-band semiconductor heterostructures*, Phys. Rev. Lett. **47**, 879 (1981)

[43] G. H. Wannier, *The structure of electronic excitation levels in insulating crystals*, Phys. Rev. **52**, 191 (1937)

[44] T. Schmielau and M. F. Pereira, *Nonequilibrium many body theory for quantum transport in terahertz quantum cascade lasers*, Appl. Phys. Lett. **95**, 231111 (2009)

[45] T. Kubis, C. Yeh, P. Vogl, A. Benz, G. Fasching, and C. Deutsch, *Theory of nonequilibrium quantum transport and energy dissipation in terahertz quantum cascade lasers*, Phys. Rev. B **79**, 195323 (2009)

[46] G. Hałdaś, A. Kolek, and I. Tralle, *Modeling of mid-infrared quantum cascade laser by means of nonequilibrium Green's functions*, IEEE J. Quantum Elect. **47**, 878 (2011)

[47] H. Kroemer, *Nonlinear space-charge domain dynamics in a semiconductor with negative differential mobility*, IEEE Trans. Electron Dev. **ED-13**, 27 (1966)

[48] M. P. Shaw, V. V. Mitin, E. Schöll, and H. L. Grubin, *The Physics of Instabilities in Solid State Electron Devices* (Plenum Press, New York, 1992)

[49] L. Esaki and L. L. Chang, *New transport phenomenon in a semiconductor "superlattice"*, Phys. Rev. Lett. **33**, 495 (1974)

[50] L. L. Bonilla and H. T. Grahn, *Non-linear dynamics of semiconductor superlattices*, Rep. Prog. Phys. **68**, 577 (2005)

[51] R. S. Dhar, S. G. Razavipour, E. Dupont, C. Xu, S. Laframboise, Z. Wasilewski, Q. Hu, and D. Ban, *Direct nanoscale imaging of evolving electric field domains in quantum structures*, Sci. Rep. **4**, 7183 (2014)

[52] M. Wienold, L. Schrottke, M. Giehler, R. Hey, and H. T. Grahn, *Nonlinear transport in quantum-cascade lasers: The role of electric-field domain formation for the laser characteristics*, J. Appl. Phys. **109**, 073112 (2011)

[53] S. L. Lu, L. Schrottke, S. W. Teitsworth, R. Hey, and H. T. Grahn, *Formation of electric-field domains in GaAs - $Al_xGa_{1-x}As$ quantum cascade laser structures*, Phys. Rev. B **73**, 033311 (2006)

[54] S. Fathololoumi, E. Dupont, Z. R. Wasilewski, C. W. I. Chan, S. G. Razavipour, S. R. Laframboise, S. Huang, Q. Hu, D. Ban, and H. C. Liu, *Effect of oscillator strength and intermediate resonance on the performance of resonant phonon-based terahertz quantum cascade lasers*, J. Appl. Phys. **113**, 113109 (2013)

[55] A. Forrer, M. Franckié, D. Stark, T. Olariu, M. Beck, J. Faist, and G. Scalari, *Photon-driven broadband emission and frequency comb RF injection locking in THz quantum cascade lasers*, ACS Photonics **7**, 784 (2020)

[56] L. L. Bonilla, I. R. Cantalapiedra, G. Gomila, and J. M. Rubí, *Asymptotic analysis of the gunn effect with realistic boundary conditions*, Phys. Rev. E **56**, 1500 (1997)

[57] F. Higuera and L. Bonilla, *Gunn instability in finite samples of gaas ii. oscillatory states in long samples*, Physica D: Nonlinear Phenomena **57**, 161 (1992)

[58] K. K. Choi, B. F. Levine, R. J. Malik, J. Walker, and C. G. Bethea, *Periodic negative conductance by sequential resonant tunneling through an expanding high-field superlattice domain*, Phys. Rev. B **35**, 4172 (1987)

[59] M. Helm, P. England, E. Colas, F. DeRosa, and S. J. Allen, *Intersubband emission from semiconductor superlattices excited by sequential resonant tunneling*, Phys. Rev. Lett. **63**, 74 (1989)

[60] Z. Y. Han, S. F. Yoon, K. Radhakrishnan, and D. H. Zhang, *Space charge buildup in tight-binding superlattices induced by electron sequential tunneling*, Superlattices and Microstructures **18**, 83 (1995)

[61] Y. A. Mityagin, V. N. Murzin, Y. A. Efimov, and G. K. Rasulova, *Sequential excited-to-excited states resonant tunneling and electric field domains in long period superlattices*, Applied Physics Letters **70**, 3008 (1997)

[62] J. Kastrup, H. T. Grahn, K. Ploog, F. Prengel, A. Wacker, and E. Schöll, *Multistability of the current voltage characteristics in doped GaAs AlAs superlattices*, Appl. Phys. Lett. **65**, 1808 (1994)

[63] J. Kastrup, R. Klann, H. T. Grahn, K. Ploog, L. L. Bonilla, J. Galán, M. Kindelan, M. Moscoso, and R. Merlin, *Self-oscillations of domains in doped GaAs AlAs superlattices*, Phys. Rev. B **52**, 13761 (1995)

[64] Y. Zhang, R. Klann, K. H. Ploog, and H. T. Grahn, *Observation of bistability in GaAs AlAs superlattices*, Applied Physics Letters **70**, 2825 (1997)

[65] T. Almqvist, D. O. Winge, E. Dupont, and A. Wacker, *Domain formation and self-sustained oscillations in quantum cascade lasers*, Eur. Phys. J. B **92**, 72 (2019)

[66] A. Yariv, *Quantum Electronics* (John Wiley & Sons, New York, 1988), 3rd edition

[67] D. O. Winge, M. Franckié, and A. Wacker, *Simulating terahertz quantum cascade lasers: Trends from samples from different labs*, Journal of Applied Physics **120**, 114302 (2016)

[68] H. G. Schuster, *Deterministic chaos: An introduction (2nd revised edition)* (VCH, Weinheim, 1988)

[69] N. J. Cornish and J. Levin, *Lyapunov timescales and black hole binaries*, Classical and Quantum Gravity **20**, 1649 (2003)

[70] M. Lecar, F. Franklin, and M. Murison, *On Predicting Long-Term Orbital Instability: A Relation Between the Lyapunov Time and Sudden Orbital Transitions*, Astronomical Journal **104**, 1230 (1992)

[71] R. Devaney and L. Devaney, *An Introduction To Chaotic Dynamical Systems, Second Edition*, Addison-Wesley advanced book program (Avalon Publishing, 1989)

[72] B. Hasselblatt and A. Katok, *A First Course in Dynamics: with a Panorama of Recent Developments* (Cambridge University Press, 2003)

[73] R. Devaney, *An introduction to chaotic dynamical systems* (Westview Press, Cambridge, Massachusetts Boulder, Colorado, 2003)

[74] G. Ohlén, S. Åberg, and P. Östborn, *Chaos* (Division of Mathematical Physics, LTH, Lund, 2006)

[75] S. C. Phatak and S. S. Rao, *Logistic map: A possible random-number generator*, Phys. Rev. E **51**, 3670 (1995)

[76] A. Carvalho, J. Langa, and J. Robinson, *Attractors for infinite-dimensional non-autonomous dynamical systems*, Applied Mathematical Sciences (Springer New York, 2012)

[77] C. Otto, K. Lüdge, and E. Schöll, *Modeling quantum dot lasers with optical feedback: sensitivity of bifurcation scenarios*, physica status solidi (b) **247**, 829 (2010)

[78] J. K. Hale and H. Koçak, *Elementary bifurcations*, in *Dynamics and Bifurcations*, pp. 25–65 (Springer, New York, NY, 1991)

[79] C. Rossant, *IPython Interactive Computing and Visualization Cookbook* (Packt Publishing, 2014)

[80] H. Kantz and T. Schreiber, *Nonlinear Time Series Analysis* (Cambridge University Press, 2003), 2nd edition

[81] A. Wolf, J. B. Swift, H. L. Swinney, and J. A. Vastano, *Determining lyapunov exponents from a time series*, Physica D: Nonlinear Phenomena **16**, 285 (1985)

[82] S. H. Strogatz, *Nonlinear Dynamics and Chaos: With Applications to Physics, Biology, Chemistry and Engineering* (Westview Press, 2000)

[83] A. M. Fraser and H. L. Swinney, *Independent coordinates for strange attractors from mutual information*, Phys. Rev. A **33**, 1134 (1986)

[84] M. B. Kennel, R. Brown, and H. D. Abarbanel, *Determining embedding dimension for phase-space reconstruction using a geometrical construction*, Phys. Rev. A **45**, 3403 (1992)

[85] N. K. Gavrilov and L. P. Šilnikov, *On three-dimensional dynamical systems close to systems with a structurally unstable homoclinic curve. i*, Mathematics of the USSR-Sbornik **17**, 467 (1972)

[86] N. K. Gavrilov and L. P. Šilnikov, *On three-dimensional dynamical systems close to systems with a structurally unstable homoclinic curve. ii*, Mathematics of the USSR-Sbornik **19**, 139 (1973)

[87] M. S. Williamson and T. M. Lenton, *Detection of bifurcations in noisy coupled systems from multiple time series*, Chaos: An Interdisciplinary Journal of Nonlinear Science **25**, 036407 (2015)

[88] A. L. Bertozzi, *Heteroclinic orbits and chaotic dynamics in planar fluid flows*, Siam J. Math. Anal. **19**, 1271 (1988)

[89] A. V. Borisov, A. O. Kazakov, , and I. R. Sataev, *Spiral chaos in the nonholonomic model of a Chaplygin top*, Regular and Chaotic Dynamics **21**, 939 (2016)

[90] E. N. Lorenz, *Deterministic Nonperiodic Flow.*, Journal of Atmospheric Sciences **20**, 130 (1963)

[91] E. L. Koschmieder, *Bénard cells and Taylor vortices*, Journal of Fluid Mechanics **253**, 722–723 (1993)

[92] C. Sparrow, *The Lorenz Equations: Bifurcations, Chaos, and Strange Attractors*, 1 (Springer, New York, NY, 1982)

[93] K. M. Cuomo and A. V. Oppenheim, *Circuit implementation of synchronized chaos with applications to communications*, Phys. Rev. Lett. **71**, 65 (1993)

[94] O. Spitz, J. Wu, M. Carras, C.-W. Wong, and F. Grillot, *Chaotic optical power dropouts driven by low frequency bias forcing in a mid-infrared quantum cascade laser*, Scientific Reports **9**, 4451 (2019)

[95] O. Spitz, A. Herdt, J. Wu, G. Maisons, M. Carras, C.-W. Wong, W. Elsäßer, and F. Grillot, *Private communication with quantum cascade laser photonic chaos*, Nature Communications **12**, 3327 (2021)

[96] K. Pusuluri, H. Ju, and A. Shilnikov, *Chaotic dynamics in neural systems*, in *Synergetics*, edited by A. Hutt and H. Haken, pp. 197–209 (Springer US, New York, NY, 2020)

[97] R. Espíndola, G. D. Valle, G. Hernández, I. Pineda, D. Muciño, P. Díaz, and S. Guijosa, *The double pendulum of variable mass: Numerical study for different cases.*, Journal of Physics: Conference Series **1221**, 012049 (2019)

[98] T. Shinbrot, C. Grebogi, J. Wisdom, and J. A. Yorke, *Chaos in a double pendulum*, American Journal of Physics **60**, 491 (1992)

[99] R. B. Levien and S. M. Tan, *Double pendulum: An experiment in chaos*, American Journal of Physics **61**, 1038 (1993)

[100] W. Singhose, D. Kim, and M. Kenison, *Input Shaping Control of Double-Pendulum Bridge Crane Oscillations*, Journal of Dynamic Systems, Measurement, and Control **130**, 034504 (2008)

[101] J. Vaughan, D. Kim, and W. Singhose, *Control of tower cranes with double-pendulum payload dynamics*, IEEE Transactions on Control Systems Technology **18**, 1345 (2010)

[102] M. Z. Rafat, M. S. Wheatland, and T. R. Bedding, *Dynamics of a double pendulum with distributed mass*, American Journal of Physics 77, 216 (2009)

[103] K. Alligood, T. Sauer, and J. Yorke, *Chaos: An Introduction to Dynamical Systems*, Textbooks in Mathematical Sciences (Springer New York, 2000)

[104] E. M. Bollt and N. Santitissadeekorn, *Applied and Computational Measurable Dynamics* (Society for Industrial and Applied Mathematics, Philadelphia, PA, 2013)

[105] G. Deskmukh, URL https : //towardsdatascience.com/modelling− the − three − body − problem − in − classical − mechanics− using − python − 9dc270ad7767, last used on February 20^{th} 2023

[106] J. Barrow-Green, A. M. Society, and L. M. Society, *Poincare and the Three Body Problem*, History of mathematics (American Mathematical Society, 1997)

[107] S. Kumar, B. S. Williams, Q. Hu, and J. L. Reno, *1.9 THz quantum-cascade lasers with one-well injector*, Appl. Phys. Lett. **88**, 121123 (2006)

[108] B. Williams, S. Kumar, Q. Hu, and J. Reno, *Resonant-phonon terahertz quantum-cascade laser operating at 2.1 THz ($\lambda \sim 141\ \mu m$)*, Electron. Lett. **40**, 431 (2004)

[109] A. Khalatpour, A. K. Paulsen, C. Deimert, Z. R. Wasilewski, and Q. Hu, *High-power portable terahertz laser systems*, Nature Photonics **15**, 16 (2021)

[110] M. S. Vitiello, G. Scamarcio, V. Spagnolo, S. S. Dhillon, and C. Sirtori, *Terahertz quantum cascade lasers with large wall-plug efficiency*, Appl. Phys. Lett. **90**, 191115 (2007)

[111] S. Fathololoumi, E. Dupont, C. Chan, Z. Wasilewski, S. Laframboise, D. Ban, A. Mátyás, C. Jirauschek, Q. Hu, and H. C. Liu, *Terahertz quantum cascade lasers operating up to $\sim$ 200 K with optimized oscillator strength and improved injection tunneling*, Opt. Express **20**, 3866 (2012)

[112] Y. B. Shi and I. Knezevic, *Nonequilibrium phonon effects in midinfrared quantum cascade lasers*, J. Appl. Phys. **116**, 123105 (2014)

[113] M. S. Vitiello, R. C. Iotti, F. Rossi, L. Mahler, A. Tredicucci, H. E. Beere, D. A. Ritchie, Q. Hu, and G. Scamarcio, *Non-equilibrium longitudinal and transverse optical phonons in terahertz quantum cascade lasers*, Appl. Phys. Lett. **100**, 091101 (2012)

[114] L. Bosco, M. Franckié, G. Scalari, M. Beck, A. Wacker, and J. Faist, *Thermoelectrically cooled thz quantum cascade laser operating up to 210 K*, Applied Physics Letters **115**, 010601 (2019)

[115] M. A. Kainz, M. P. Semtsiv, G. Tsianos, S. Kurlov, W. T. Masselink, S. Schönhuber, H. Detz, W. Schrenk, K. Unterrainer, G. Strasser, and A. M. Andrews, *Thermoelectric-cooled terahertz quantum cascade lasers*, Opt. Express **27**, 20688 (2019)

Part II

Research Papers

Scientific publications

Author contributions

Paper I: Chaotic Behaviour of Quantum Cascade Lasers at Ignition

D. E. Önder, A. A. S. Kalaee, D. O. Winge, A. Wacker, Communications in Nonlinear Science and Numerical Simulation, **103**, 105952 (2021)

Doi: 10.1016/j.cnsns.2021.105952

As the corresponding author, I wrote the first draft and provided all the numerical data from the NEGF package and the domain model implemented by David Winge. I came up with the idea of constructing bifurcation and phase plots to strengthen our identification of chaotic behaviour. The model and the calculations to extract Lyapunov exponent in Fig.10 were done by Alex Arash Sand Kalaee.

Paper II: Analysis of High-Performing Terahertz Quantum Cascade Lasers

Viktor Rindert, Ekin Önder, Andreas Wacker, Physical Review Applied **18**, L041001 (2022), [Letter Section]

Doi: 10.1103/PhysRevApplied.18.L041001

In this paper, I co-supervised Viktor Rindert and helped him to produce the data. I contributed to the conceptualization and improving the figures. I also contributed to the writing of the manuscript.

Paper III: Frequency Modulations due to Domain Dynamics in Terahertz Quantum Cascade Lasers

E. Önder, D. O. Winge, M. Franckié, A. Forrer, U. Senica, G. Scalari, and Andreas Wacker, Journal of Applied Physics, **133**, 123101 (2023), [Featured article]

Doi: 10.1063/5.0137716

This project was initiated by myself together with Martin Franckié. I produced all the simulated data using the NEGF package and the domain model and wrote the first draft. The experimental data was processed by Andres Forrer and Urban Senica.